

# Multifrequency Polarimetric Synthetic Aperture Radar Observations of Sea Ice

MARK R. DRINKWATER AND R. KWOK

*Jet Propulsion Laboratory, California Institute of Technology, Pasadena*

D. P. WINEBRENNER

*Polar Science Center, Applied Physics Laboratory, University of Washington, Seattle*

E. RIGNOT

*Jet Propulsion Laboratory, California Institute of Technology, Pasadena*

The first known fully polarimetric airborne synthetic aperture radar (SAR) data set of sea ice is introduced. Images were acquired in the Beaufort, Bering and Chukchi seas in March 1988, during a campaign for validation of Defense Meteorological Satellite Program Special Sensor Microwave Imager radiometer ice products. Statistics of the magnitude, phase and polarization of complex backscattered signals recorded by the Jet Propulsion Laboratory three-frequency SAR are examined in detail for various scenes with different ice characteristics. The full Stokes matrix information generated from C, L, and P band data characterize the scattering behavior of different ice types. Polarization ratios and phase differences between linear copolarized returns are used for discrimination between particular image features and mechanisms are suggested for the observed polarimetric characteristics. Results indicate that combinations of frequency and polarization enhance current capability to distinguish ice of different properties using single frequency, fixed polarization microwave radar. A specific example is the polarimetric identification of new ice formation which may not be easily distinguished in ERS-1 5.3GHz, VV polarization SAR data. Such findings are consistent with theoretical model simulations of scattering characteristics of sea ice. Overall, these preliminary results demonstrate that radar polarimetry will likely add a new dimension to our current capability for extracting geophysically important ice variables using radar remote sensing methods.

## 1. INTRODUCTION

The formation of sea ice plays a delicate role in modulating both regional and global climate because of its effect upon the surface heat exchange between atmosphere and ocean. Sea ice markedly alters the surface albedo, modifies the surface roughness, and insulates the ocean from the atmosphere. During ice formation and growth, the effects of brine rejection play an important part in modifying the salinity and buoyancy of water masses. Hence sea ice affects the radiant and turbulent heat exchange and the momentum transfer between the ocean and the atmosphere, as well as the vertical and horizontal mixing and redistribution of salt in the polar oceans. In locations of substantial annual ice production these fluxes may conceivably control production of intermediate and bottom waters of the world oceans and the global atmospheric heat budget.

Varying sea ice conditions affect the radiative properties of the surface over the entire spectral range between visible and microwave wavelengths. It is in the latter, the microwave or centimeter-scale wavelength range (gigahertz frequencies), that emitted and scattered surface radiation is least attenuated by the atmosphere, and of course, is independent of daylight. In the last decade, the community using microwave remote sensing techniques to address the problems of obtaining synoptic sea ice geophysical information in

the remote polar regions has grown considerably in size and sophistication. The technique of synthesizing a radar aperture has enabled the development of high-resolution active microwave systems which can obtain wide-area coverage, without restriction. Synthetic aperture radar (SAR) has received considerable interest in the geoscience community since the brief Seasat satellite mission in 1978. It is perhaps indicative of the potential capability of future spaceborne SAR for sea ice remote sensing that many people have developed applications in this area.

SAR data have been used extensively for the study of ice kinematics and deformation [Leberl *et al.*, 1983; Curlander *et al.*, 1985; Fily and Rothrock, 1986, 1990; Carsey and Holt, 1987; Drinkwater and Squire, 1989]. Techniques and algorithms to derive ice motion information have developed to the point where routine automated tracking and ice floe motion vector mapping will be carried out on future European Remote Sensing Satellite (ERS-1) images received at the Alaska SAR Facility [Kwok *et al.*, 1990]. The calculation of the fractional coverage of significant ice types is instrumental in estimation of the heat balance of the polar regions. Often, classes of old or multiyear ice, first-year ice, thin first-year ice and open water are used as a proxy indicator of ice thickness. SAR images have thus been widely applied in the estimation of ice types and their areal coverage [Martin *et al.*, 1987; Burns *et al.*, 1987], but the chief concern remains that we do not yet have a complete record of the seasonal changes in the backscatter signatures of these ice types. Operational algorithms have been developed for the

Copyright 1991 by the American Geophysical Union.

Paper number 91JC01915.  
0148-0227/91/91JC-01915\$05.00

TABLE 1. JPL AIRSAR Sensor Description and Specifications

	Description
Sensor	multifrequency synthetic aperture radar
Aircraft	NASA DC-8 aircraft
Frequencies, GHz	5.3 (C band), 1.25 (L band), 0.44 (P band)
Wavelength, m	0.056, 0.24, 0.68
Polarization (linear)	HH, HV, VV, VH
Look angle range, deg	0–70
Nominal altitude, m	9000
Nominal ground speed, knots (m s <sup>-1</sup> )	420 (215) for best SNR

classification of ice types in satellite images [Holt *et al.*, 1989, 1990], and it is anticipated that these algorithms will become more robust as our understanding of seasonal changes in the microwave signatures improves. Most recently, the influence of regional ice properties (including ice concentration, floe size, and roughness distribution) upon the SAR signal have been investigated as a source of information on the spatial variability in the atmospheric drag coefficient [Burns, 1990]. Accurate estimates of the drag coefficient are required not only for investigations of the transfer of momentum from wind to ice, but also for more accurate parameterization of the wind stress upon sea ice in air-sea-ice dynamic-thermodynamic models.

The value of SAR data in geophysical investigations would be significantly enhanced by more directly linking variations in microwave signature of sea ice to quantities of direct geophysical interest (e.g., the thickness of new ice and snow cover). Efforts to establish such links have increased in recent years and have involved quasi-controlled experiments on artificially grown sea ice [Bredow *et al.*, 1989], ground-based field measurements [Onstott *et al.*, 1987], coordinated airborne and shipborne campaigns [Drinkwater, 1989; Livingstone and Drinkwater, 1991], as well as theoretical modeling work [Winebrenner *et al.*, 1989]. From the most recent of such efforts, there are indications that stronger connections between SAR signatures and geophysical variables may be established using multichannel SAR data, i.e., measurements made simultaneously at more than one frequency and/or polarization. The value of multichannel SAR data has been shown in other geophysical settings by van Zyl [1989] and Zebker *et al.* [1987], among others [Ulaby and Elachi, 1990], but such data for sea ice have only very recently become available.

Our purpose in this paper is to present some of the first examples of multifrequency, polarimetric SAR data for sea ice together with an initial examination of signature variations within and between apparently different ice types in the images. From the observations, we identify regularities in the signatures as well as variations that may be useful for remote sensing of geophysically interesting quantities. We begin in the next section with an overview of the locations and conditions under which the data were acquired. Following this is a brief review of polarimetry, including precise definitions for the signatures we compute and use to compare different types of ice. We then examine signatures as a function of apparent ice type, such as old ice, thick first-year ice and leads; apparent ice type is determined by visual interpretation of the SAR images. In some cases, ancillary information such as airborne passive microwave imagery

and some very limited ground observations are available to aid interpretation, while in others previous experience with SAR imagery is the only guide available. In the discussion section we compare signature variations across ice types as functions of frequency and highlight variations which require further investigation.

## 2. POLARIMETRY DATA SET

### Background

During March 1988, multifrequency SAR polarimetric data were acquired over Beaufort, Chukchi, and Bering Sea ice using the NASA DC-8 airborne laboratory [Cavalieri, 1988]. Radar polarimetry refers here to an instrumental technique which allows determination of the complex backscatter coefficients of radar echoes for all transmit and receive polarization states. High-resolution, imaging polarimetry, such as that discussed in this paper, enables the measurement of the received amplitude and phase of echoes at all polarizations. The Jet Propulsion Laboratory (JPL) airborne SAR (AIRSAR) operates simultaneously at P, L, and C band (i.e., at wavelengths of  $\lambda = 0.68, 0.24$ , and  $0.056$  m), transmitting and receiving from separate antennas in four linear polarization combinations, and digitally recording the complex scattered wave (see Table 1). Conventional monostatic imaging radars operate with a single, fixed-polarization antenna: in this way it has been possible to record only a single scattering coefficient for a rigid transmit and receive polarization. The JPL radar polarimeter, however, enables measurement of the complete polarization

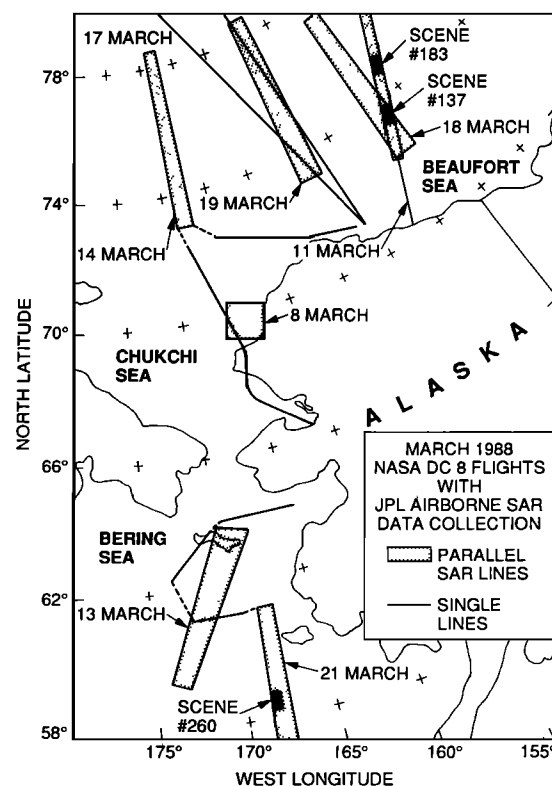


Fig. 1. Map showing data collection during March 1988 airborne campaign, and indicating locations of scenes used in the analysis.

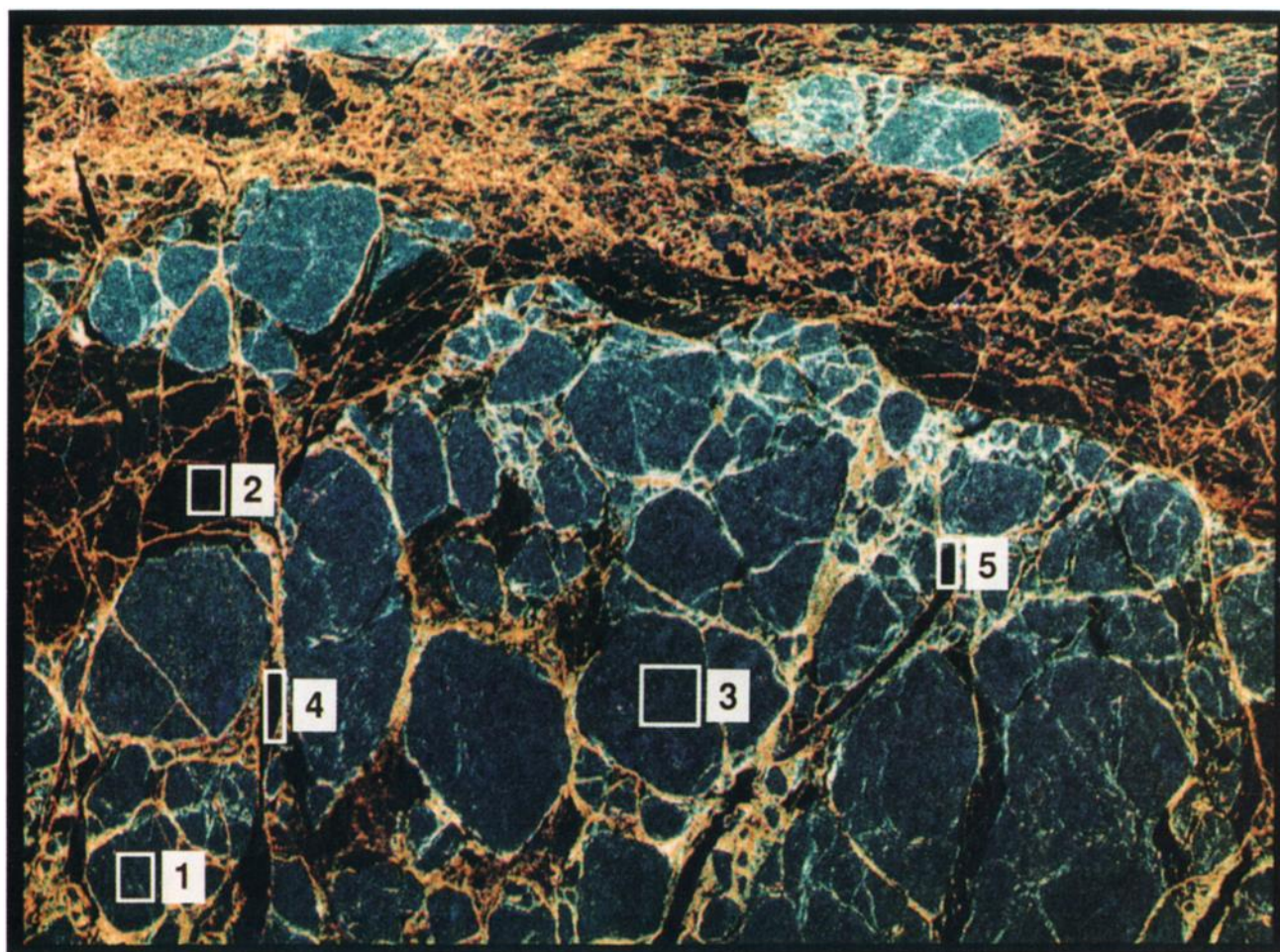


Plate 1. Scene 137: Beaufort Sea three-frequency power image acquired at a location  $73^{\circ}13.4'N$ ,  $142^{\circ}1.1'W$  at 1721:26 UT (i.e., 0821:26 LT) on March 11, 1988.

signature of every resolution element of an image, thus providing a greater capability for target discrimination than was the case previously using conventional SAR data and related image analysis techniques.

#### Scene Locations

Image data discussed in this paper are scenes which typify the ice conditions which were present in the Beaufort Sea and the Bering Sea in March 1988 (Figure 1). These images highlight a variety of ice types which contribute to the signatures described in the following sections. Figure 1 indicates the locations of the radar scenes shown in Plates 1, 2, and 3. Scene 137 (Plate 1) was acquired in the Beaufort Sea at 0821:26 local time (LT) on March 11, 1988. Scene 183 (Plate 2) was acquired further north at 0826:39 LT, along the same flight leg. The third and final scene, 260 (Plate 3), was acquired some 2 weeks later in the Bering Sea, on March 21 at 1012:07 LT. Each color radar image is displayed in the standard JPL format as a three-frequency overlay. These red, green, and blue color composites represent the P, L, and C band frequency responses with each individual pixel intensity modulated by total backscattered power.

#### Weather and Ice Conditions

**Beaufort Sea.** Weather and sea ice data were collected in March 1988 within a 150-km radius of the Applied Physics

Laboratory (APL) drifting ice station (APLIS '88), approximately 400 km north of Prudhoe Bay, Alaska. Daily air temperatures, atmospheric pressure, wind speed, and wind direction were recorded at the location of the ice camp and are reported by *Wen et al.* [1989]. These records provide the most reliable description of the mesoscale meteorological conditions in the region where aircraft remotely sensed data were acquired. On March 11, scenes 137 and 183 were taken on a flight leg extending northeastward from the coast of Alaska to the northern tip of Ellesmere Island [*Cavalieri*, 1988; *Cavalieri et al.*, 1991]. The location of APLIS '88 (from Global Positioning System) at the times of the data acquisition, was approximately  $72^{\circ}40'N$ ,  $143^{\circ}42.57'W$ , and thus the distance of the two Beaufort Sea scenes from the ice camp is approximately 80 km and 148 km, on bearings of  $39^{\circ}$  and  $28^{\circ}$ , respectively. Wind speeds on March 11 at the ice camp reportedly varied between 1 and  $5 \text{ m s}^{-1}$  from the south [*Wen et al.*, 1989], due to a low-pressure system located over central Alaska. Air temperatures fluctuated between  $-12^{\circ}$  and  $-18^{\circ}\text{C}$  on March 11, while the mean temperature over the preceding 4-day period was  $-16^{\circ}\text{C}$ . Two brief periods of temperatures below  $-25^{\circ}\text{C}$  were experienced on March 3–5 and March 8. The weather station did not automatically record air pressure at this stage, but weather charts indicate pressures between 1000 and 1020 mbar in the region, which corresponded with a northeastward extension of a low pressure system tracking over central Alaska.



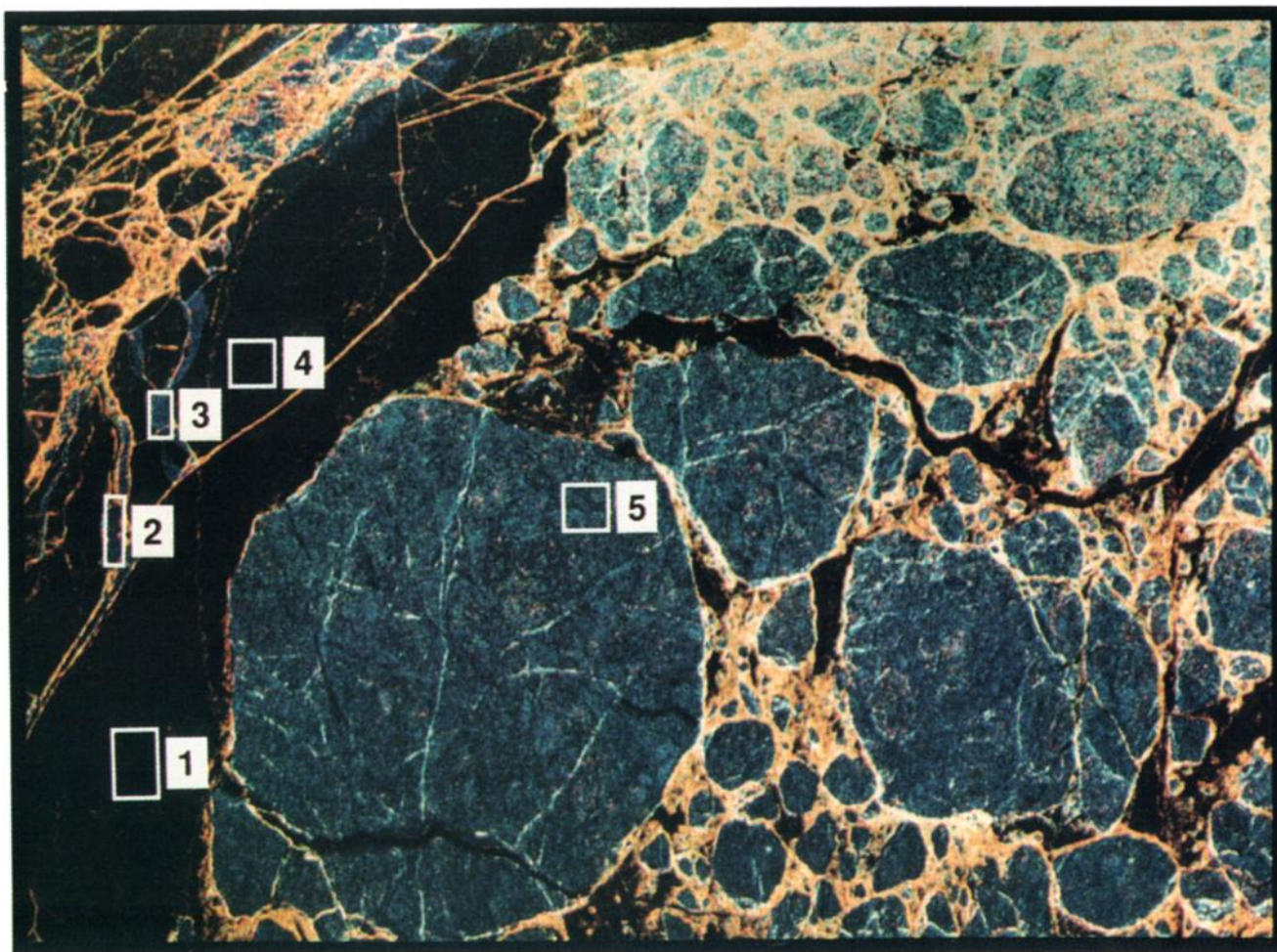


Plate 2. Scene 183: Beaufort Sea three-frequency power image acquired on March 11, 1988, at 73°48.9'N, 141°2.7'W at 1726:39 UT (i.e., 0826:39 LT).

Ice conditions comprised a mixture of first-year (FY) and multiyear (MY) ice forms in this region of transition between the polar pack and younger nearshore ice [Drinkwater *et al.*, 1991; Cavalieri *et al.*, submitted]. The combination of young and old ice typically consisted of large, rounded MY floes surrounded by a matrix of deformed FY ice. Narrow, protected frozen leads, separating older ice floes, often remained undeformed, demonstrating that they had undergone little convergence since freeze-up. Exposed areas of somewhat older FY ice, however, indicate significant deformation by the ridging and rubble piles which crisscross many surfaces.

APLIS '88 investigators noted the characteristics of the sea ice in their vicinity. Multiyear ice was commonly snow covered and hummocked to amplitudes of 6.0 m. First-year ice separating these MY floes had thicknesses ranging from 1.5 m to 2.4 m and typically had a dry snow cover of variable depth with a mean of 15 cm [Wen *et al.*, 1989]. Subsurface conditions were noted by divers during APLIS '88, and crude measurements resulted in the conclusion that ice growth rates in the FY ice areas were spatially quite variable. Underside topography resulting from this variability demonstrated sinusoidal undulations with amplitudes of 3.7 cm and wavelengths of 8.5 m, with uniformity of both wavelength and orientation. Bottom roughness appeared to correspond with surface snow features such as sastrugi or

snow dunes and is thought to result from the modulation of freezing rates as a function of the insulating snow cover [Wen *et al.*, 1989]. Congelation ice growth rates beneath flat portions of the FY ice were about  $0.5 \text{ cm d}^{-1}$ . The underside of deformed FY sea ice contrasted markedly with that of older ice surviving the summer melt. Keels only a few months old in the young ice retained their original structure with randomly oriented blocks of ice, while their older counterparts in MY ice were commonly polished and rounded, lacking any recognizable signs of block structure.

Ice drift in the location of scenes 137 and 183, was observed to be largely westward during the period of observations. Drift speeds recorded at APLIS '88 indicated that bouts of rapid ice motion and deformation were correlated with periods of high wind speeds. Prior to the images in Plates 2 and 3, winds of approximately  $7\text{--}8 \text{ ms}^{-1}$  had been recorded, and the sea ice drift apparently responded by peaking at  $0.32 \text{ m s}^{-1}$  on 10 March: this was the highest ice drift velocity recorded at APLIS '88 during the months of March and April. Divergent ice motion was responsible for many new cracks and leads imaged on March 11, and new ice formations were consequently observed in scenes where leads were rapidly freezing under the cold conditions.

From the surface information recorded by Wen *et al.* [1989] on the physical and chemical properties of the local ice forms, general mean dielectric properties are calculated



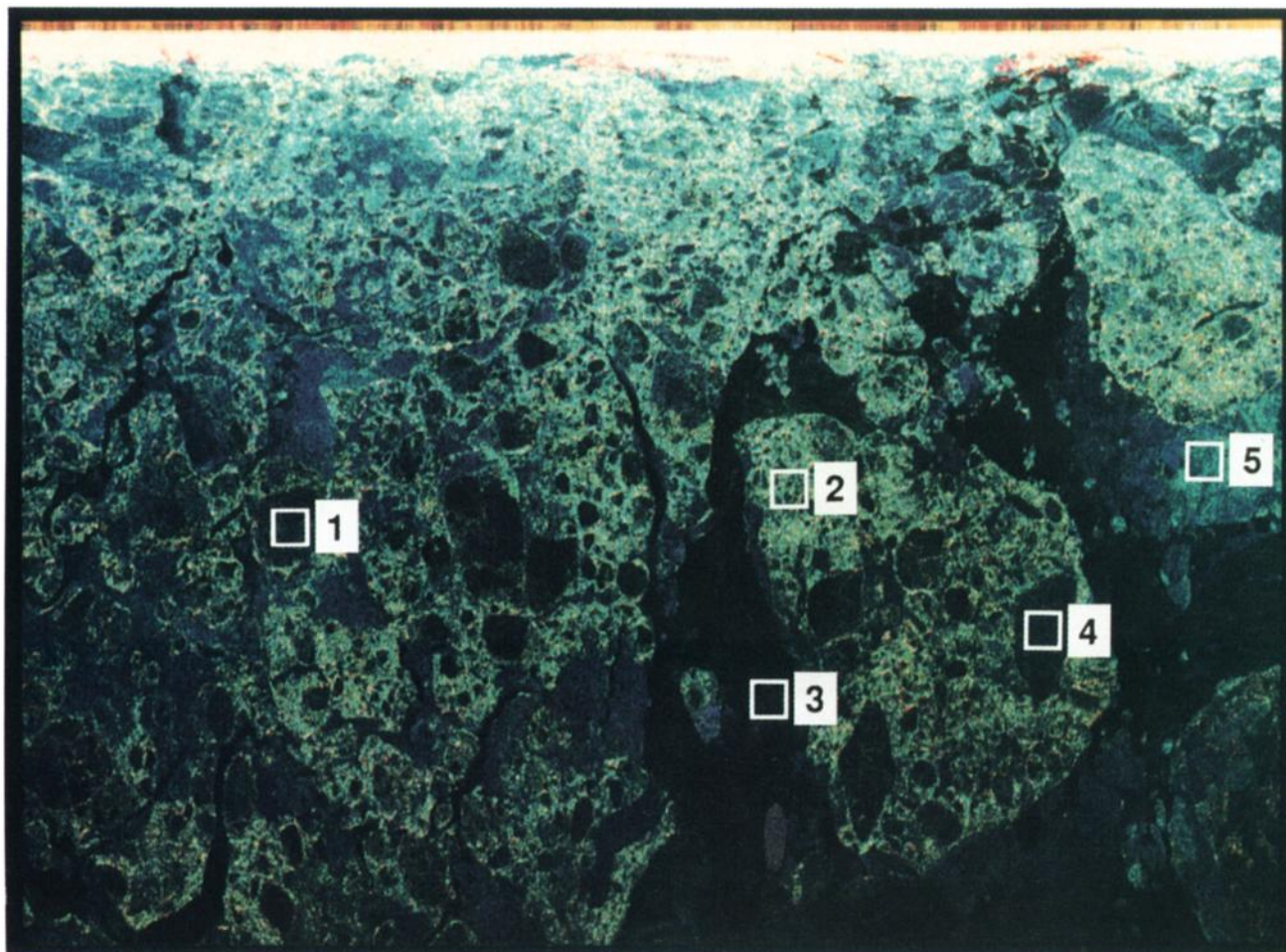


Plate 3. Scene 260: Bering Sea three-frequency power image acquired at 0512:07 UT on March 22, 1988 (i.e., 2012:07 LT on March 21) at 58°27.3'N, 167°35.7'W.

using the phase relations for sea ice [Frankenstein and Garner, 1967] and empirical formulae [Vant *et al.*, 1978]. Parameters used to derive the dielectric properties are listed in Table 2a, and the resulting dielectric constants shown in Table 2b. These general properties are used later in the paper to estimate the expected values of polarimetric parameters, using a simple theoretical model described by Winebrenner *et al.* [1989].

**Bering Sea.** Meteorological data for the area encompassing scene 260 in the Bering Sea were acquired by weather stations located on St. Paul Island and in the Aleutians. Parameters recorded indicate that during the latter period of the experiment a deep low-pressure system swept across the north slope of Alaska, leaving blowing snow and falling temperatures. As high pressure developed in its wake, storm systems resumed their usual track into the Gulf of Alaska, thereby maintaining a cold, brisk northerly airflow over the Bering Sea. During the week of March 20–26 the cold front pushed southward, and St. Paul Island (57°10'N, 170°20'W) in the central Bering Sea experienced temperatures 14° below the monthly norm of between –5° and –16°C. Other weather stations further south in the Aleutians recorded unseasonably cold temperatures of –15°C, some 10°C or more below normal.

General ice conditions were fairly typical for March [Cavalieri *et al.*, 1986, submitted; MIZEX-West Study Group, 1983], with a variety of well-deformed FY ice forms

and individual floe sizes ranging up to 1 km in diameter. Observations from NOAA satellite advanced very high resolution radiometer (AVHRR) images indicate heterogeneous mixtures of FY ice types, and higher-resolution radar images confirm a congealment of broken and deformed FY ice refrozen together in large aggregated units. Large, thick FY ice floes were observed during flights south of St. Matthew Island on March 13, but flights later in the month did not encounter such large floe sizes. It is evident that by March 22, most large floes had been fractured into relatively smaller units. In the radar images, undeformed thick FY floes clearly stand out as dark (i.e., low backscatter) targets in a well-deformed matrix which gives a contrasting, bright (i.e., high backscatter) response. Such SAR image characteristics have been documented previously by Drinkwater [1989] under Labrador Sea marginal ice conditions.

Northerly winds had a significant impact upon ice conditions imaged in many areas during the latter part of the experiment (see Figure 1 for locations). NOAA and Landsat satellite images indicate that previously observed polynyas again developed on the southern side of St. Lawrence and St. Matthew islands [Cavalieri *et al.*, 1986], thereby promoting extensive growth of thin and new ice forms in those areas of open water. Winds advected the ice edge south, and banding and large areas of open water developed within the marginal ice zone due to the strong ice divergence. Lower

TABLE 2a. March Sea Ice Properties for Beaufort and Bering Sea Ice Forms

Type	Density, g cm <sup>-3</sup>	Temperature, °C	Salinity, ‰	Brine Volume
<i>Beaufort Sea</i>				
Multiyear	0.80	-10.0	0.0	0.000
Thick FY	0.92	-10.0	8.5	0.047
Young ice	0.85	-8.0	15.0	0.092
<i>Bering Sea</i>				
Thick FY	0.90	-10.0	10.0	0.054
Young ice	0.85	-8.0	15.0	0.092
Sea water		-2.0	32.0	

March sea ice properties from descriptions of Beaufort Sea FY ice parameters by Wen *et al.* (1989), and typical Bering Sea ice parameters documented during BESEX [Ramseier *et al.*, 1975] and MIZEX '83 [MIZEX-West Study Group, 1983; Grenfell, 1986]. Thick FY ice values assume a snow depth of 10–15 cm, and the young ice values assume no snow cover or frost flowers.

than normal temperatures thus resulted in large areas of new and young ice formation in the central Bering Sea.

Table 2a shows typical values for the characteristics of thick first-year ice in the Bering Sea, as observed in the month of March during the Bering Sea Experiment (BESEX) [Ramseier *et al.*, 1975] and the 1983 Marginal Ice Zone Experiment (MIZEX '83) [MIZEX-West Study Group, 1983; Cavalieri *et al.*, 1986; Grenfell, 1986]. Climatic conditions recorded during the special sensor microwave imager (SSM/I) validation campaign in March 1988 were somewhat similar to the situation experienced in 1973 and 1983 (Cavalieri *et al.*, submitted), and the resulting ice properties are generally expected to be similar.

### 3. RADAR POLARIMETRY BACKGROUND

#### Definitions and Polarimetric Data Description

For efficient data storage, the polarimetric data distributed by JPL are encoded in a compressed Stokes matrix format [Zebker and Lou, 1990]. The reconstructed Stokes matrix at each spatial sample is a  $4 \times 4$  symmetric real matrix representing the polarimetric backscattering properties for an area of the surface. For the purposes of describing the signatures in this paper, several quantities are derived from the scattering matrix at each frequency. The polarimetric feature vector  $X$

$$X = \begin{bmatrix} S_{HH} \\ S_{HV} \\ S_{VV} \\ S_{VH} \end{bmatrix} \quad (1)$$

is used to define the polarimetric or Stokes parameters recorded by the SAR for any given pixel.  $S_{xy}$  refers to the complex scattering amplitude for  $x$ -transmit,  $y$ -receive polarizations and H and V signify horizontal and vertical polarization, respectively. From  $X$  and the full Stokes matrix, the following basic polarimetric quantities are derived for each individual pixel:

$$A_{HH} = |S_{HH}| \quad (2a)$$

$$A_{VV} = |S_{VV}| \quad (2b)$$

$$A_{HV} = |S_{HV}| \quad (2c)$$

$$r_{HH/VV} = \frac{(S_{HH}S_{HH}^*)}{(S_{VV}S_{VV}^*)} \quad (3a)$$

$$r_{HH/HV} = \frac{(S_{HH}S_{HV}^*)}{(S_{HV}S_{HV}^*)} \quad (3b)$$

$$\Delta\phi_{HH-VV} = \angle S_{HH}S_{VV}^* \quad (4a)$$

$$\Delta\phi_{HH-HV} = \angle S_{HH}S_{HV}^* \quad (4b)$$

where  $A_{xy}$  is the scattered amplitude for the receive ( $x$ ) and transmit ( $y$ ) polarization combination denoted;  $r_{HH/VV}$  is the ratio of the copolarized returns, and  $r_{HH/HV}$  is the ratio of the cross polarized and copolarized returns,  $\angle$  denotes the phase difference of the complex quantities in the argument, and an asterisk signifies the complex conjugate.  $\Delta\phi_{HH-VV}$  is the phase difference between the two copolarized channels, and  $\Delta\phi_{HH-HV}$  is the phase difference between the cross-polarized and one of the copolarized channels (in this case HH), where

$$S_{HH}S_{VV}^* = A_{HH}A_{VV}e^{i\Delta\phi_{HH-VV}} \quad (5a)$$

$$S_{HH}S_{HV}^* = A_{HH}A_{HV}e^{i\Delta\phi_{HH-HV}} \quad (5b)$$

For the purposes of this paper, targets are identified within a scene, and sample areas are chosen accordingly. Typically, these targets comprise several hundred pixels or more. All polarimetric quantities defined above are extracted from pixels within the sample windows shown in Plates 1–3. Additional statistics  $\mu_{HH/VV}$  and  $\sigma_{HH/VV}$  are then calculated to describe the mean and standard deviation of the sampled copolar amplitude ratios; and  $\phi_{HH-VV}$  and  $\sigma_{\phi_{HH-VV}}$  are the mean and standard deviation of the sampled copolar phase differences, respectively.

#### Polarimetric Scene Calibration

In order to utilize variations in the aforementioned polarimetric quantities for target characterization purposes, one

TABLE 2b. Frequency-Dependent Sea Ice Dielectric Properties, Estimated Using Values From Table 2a

Frequency, GHz	MY Ice	Beaufort FY	Bering FY	New	Water
0.4	2.9 - j0.0	3.83 - j0.38	3.93 - j0.43	4.39 - j0.70	77.1 - j122.8
1.0	2.9 - j0.0	3.54 - j0.28	3.61 - j0.31	3.95 - j0.50	76.3 - j55.97
4.0	2.9 - j0.0	3.39 - j0.18	3.44 - j0.20	3.71 - j0.33	64.7 - j39.35

After Vant *et al.* [1978, Table IV]. Here  $j$  is the square root of  $-1$ .

must consider the accuracy of the radar measurements. In polarimetric measurements, gain imbalance and cross talk (leakage) between the H and V polarized radar channels would affect the polarimetric ratios, whereas uncertainty in the phase relationship between channels of the radar can lead to offset in the relative phase measurements.

In the absence of external calibration targets (targets with known polarimetric ratios), it is difficult to determine the between-scene performance of the instrument. This is especially true of SAR imaging in remote drifting sea ice regions, where deployment of such targets is a logistically difficult task. The available information on the polarimetric characteristics of the radar flown in the 1988 Alaska campaign indicate that the instrument was quite stable at L band, although less so at C and P bands. Polarimetric calibration of the radar was assessed by *Freeman* [1990] during an over-flight of trihedral corner reflectors deployed on March 13 near Fairbanks, Alaska. From trihedral measurements, the gain imbalance (i.e.,  $r_{HH/VV}$  offset) between the two copolarized channels was 1.8 dB and  $-0.6$  dB for C and L bands, respectively. Cross-channel isolation  $r_{HH/HV}$  of C and L bands were 27 dB and 17 dB, respectively, and this affects the sensitivity of the cross-polarized (HV) returns from the sea ice. The relative stability of the C and L band radars is borne out by the relative consistency of the polarimetric measurements over FY and MY ice during the campaign. The performance of the P band polarimeter was uncertain owing to the low cross sections of the trihedrals at this wavelength and was not assessed during the March 13 experiment described by *Freeman* [1990]. Nonetheless, general values may be drawn from calibrations undertaken before and after the Alaska flights which indicate a mean  $r_{HH/VV}$  offset of  $-0.2$  dB and cross-channel isolation of 22 dB.

Phase calibration is a required step in the utilization of the imaging polarimeter data owing to instrument-induced errors in the phase relationship between the radar channels. This error is manifested in the polarization signatures as skewed or shifted peaks. Calibration is thus accomplished by selecting an in-scene target where the scattered HH-VV phase difference (i.e.,  $\Delta\phi_{HH-VV}$ ) is known or can be presumed and by using this knowledge to remove the phase offset between the channels for the entire scene. A summary of this phase calibration approach is detailed by *Zebker and Lou* [1990]. Sample windows within a MY ice floe in scenes 137 and 183 (Plates 1 and 2) were selected as polarimetric phase references with zero mean phase difference (i.e.,  $\bar{\phi}_{HH-VV} = 0$ ). Examination of the polarimetric phase difference distributions in both MY and FY ice indicate that they are as a result both approximately the same, with  $\bar{\phi}_{HH-VV} \approx 0$ , and that either FY or MY ice floes could have been selected as calibration reference targets. After calibration, the polarimetric signatures of FY signatures are characteristic of scattering from slightly rough surfaces (see results), which is indicative that the phase calibrations applied are effective in removing system-induced channel phase errors. The resulting estimated precision for the between-channel copolar phase difference  $\Delta\phi_{HH-VV}$  is thus  $\pm 5^\circ$ . Supporting evidence is provided from phase sensitivity tests performed on scene 183 using multiple samples of MY ice with increasing incidence angle (in the range  $40^\circ < \theta < 51^\circ$ ). These results indicate that the maximum range of variability in  $\bar{\phi}_{HH-VV}$  after phase calibration is  $2.32^\circ$ , for all three frequencies.

### Polarization Signatures and Statistics

From the Stokes matrix data the polarization signature of any given sample window can be synthesized [*Zebker et al.*, 1987]. Though the complex signals are recorded at the fixed combinations of polarization described in Table 1, enough information is retained to reconstruct the specific polarization of the backscatter in each image pixel [*Evans et al.*, 1988]. In this manner, any combination of synthetic antenna polarization can be selected for transmit and receive with the resulting mixture of polarized backscattered power displayed in graphical form. Examples extracted from FY and MY ice are shown in Figures 2 and 3; and the plots illustrated are normalized (such that the 1, 1 element of the Stokes matrix is unity), three-dimensional representations of the co- or cross-polarized radar cross sections of these features at a given incidence angle ( $\theta$ ). Copolarized signatures are obtained by setting the receive polarization equal to that transmitted and by measuring the backscattered power as the orientation and ellipticity angles describing the polarization are varied [*Zebker et al.*, 1987]. In a similar manner, the cross-polarized signature is obtained by constraining the receive antenna ellipticity to be the negative of the transmitted ellipticity, and the receive antenna orientation to that of the transmit antenna plus  $90^\circ$  [*Zebker et al.*, 1987; *van Zyl et al.*, 1987; *van Zyl and Zebker*, 1990]. Two statistics which characterize these signatures, and which may be derived from the Stokes matrices, are the coefficient of variation  $\gamma$ , defined as

$$\gamma = \frac{P_{\min}}{P_{\max}} \quad (6)$$

and the fractional polarization  $f_p$ ,

$$f_p = \frac{P_{\max} - P_{\min}}{P_{\max} + P_{\min}} \quad (7)$$

where  $P_{\min}$  and  $P_{\max}$  are the minimum and maximum power over both the co- and cross-polarized signatures. Values of  $\gamma$  and  $f_p$  relate to the heterogeneity of the scattering mechanisms in a sample area and the fraction of polarized returns. High values for the coefficient of variation  $\gamma$ , can be caused by a combination of (1) multiple scattering, (2) inhomogeneity in the scattering mechanisms within the sample, and (3) a low signal-to-noise ratio (SNR). Unpolarized returns constitute a polarization pedestal which varies as a function of  $f_p$ . The more the component polarizations in a sample box differ, the less the expected difference between  $P_{\max}$  and  $P_{\min}$  values in the resulting signature. A target area with diffuse scattering properties usually produces a value of  $\gamma$  close to unity (i.e., no preferential polarization; the scattered signal is independent of antenna configuration) and low  $f_p$  [*Evans et al.*, 1988]. When  $f_p = 0$ , the average return is completely unpolarized, and varying the antenna polarization will not change the average backscattered power. In contrast, for ocean surfaces where Bragg scattering is dominant,  $\gamma$  tends to 0 and  $f_p$  values are typically high. When  $f_p = 1.0$ , the average return is completely polarized and variations in antenna polarization will cause a relatively large variation in average backscattered power. All examples from sea ice observed in March 1988 fall into the latter category of targets with preferential scattering characteristics, and demonstrate values of  $0.01 \leq \gamma \leq 0.10$  and  $0.82 \leq$

Scene title BEAUFORT SEA - C BAND - 183

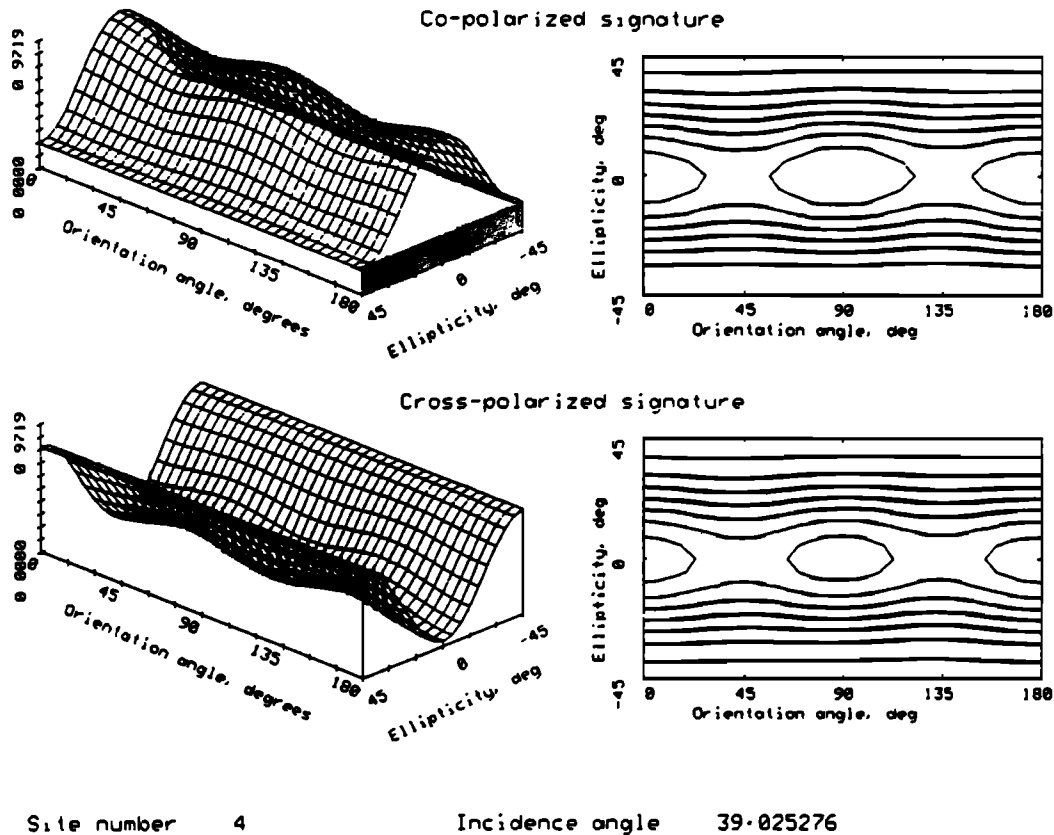


Fig. 2. C band copolarized and cross-polarized signatures extracted from sample 183-4 (thick first-year (TFY) ice) at an incidence angle of  $39^\circ$ . The signature indicates a typical rough surface scattering example where geometric optics scattering is presumed dominant. Unpolarized returns constitute the shaded pedestal in the copolarized signature.

$f_p \leq 0.98$  (see Table 3). Small values of  $\gamma$  and high values of  $f_p$  demonstrate that there is some degree of homogeneity in the scattering mechanisms within sampled targets, that multiple scattering appears to be of secondary importance, and also that the signal-to-noise ratio of the measurements is large.

#### 4. POLARIMETRIC SIGNATURES OF SEA ICE

In this section, we examine the polarimetric signatures at P, L, and C bands as functions of apparent ice type. This method is designed to illustrate the within-class similarity (or variability) in signatures extracted from various targets with the same apparent image characteristics. Then we further examine the between-class variability of signatures, to indicate the unique characteristics of some of the signatures, and ways in which ice classes may be discriminated using polarimetric statistics. For the purposes of illustration, the three-frequency images shown in Plates 1–3 will be used to extract signature examples.

Prior to data analysis it was imperative to establish the noise floor of the instrument, and the degree to which polarimetric signatures from low-backscatter features could be influenced by system noise. The noise equivalent value for the backscatter ( $\sigma^0$ ) is  $-35$  dB, and the lowest value of observed backscatter from any target signatures subsequently analyzed was approximately  $-20$  dB. Thus there

exists a margin of some 10 dB above the noise floor equivalent of the radar; none of the examples illustrated in the following sections appear to have noise-induced attributes.

#### Old Ice Signatures

As typical areas of old ice, we have selected regions 1 and 3 of image 137 (hereinafter denoted as 137-1 and 137-3, respectively) in Plate 1 and region 5 of image 183 (denoted 183-5) in Plate 2. From the bright return at C band (and hence the blue hue), the rounded floe edges and other morphological clues, it appears that the selected areas indeed contain ice that has survived one or more summers. Thus the upper 10 to 30 cm of ice in these areas is likely to contain many millimeter-sized air bubbles or inclusions and thus likely to be of low density (in the documented range  $0.75$ – $0.85$  g cm $^{-3}$ ). In the Beaufort Sea in March, we expect such floes to be covered by between 5 and 20 cm of dry, fine-grained snow. This is consistent with observations at the APL ice camp some 150 km distant [Wen *et al.*, 1989].

If scattering losses within the ice are ignored and the ice properties given in Table 2a are representative of the ice imaged, the approximate dielectric properties in Table 2b can be used to estimate the maximum penetration depth within the sea ice. A propagation distance in MY ice can be calculated, for which the incident intensity is reduced by  $e^{-1}$  [Onstott *et al.*, 1987]: the result is a potential penetration



Scene title BEAUFORT SEA - L BAND - 137

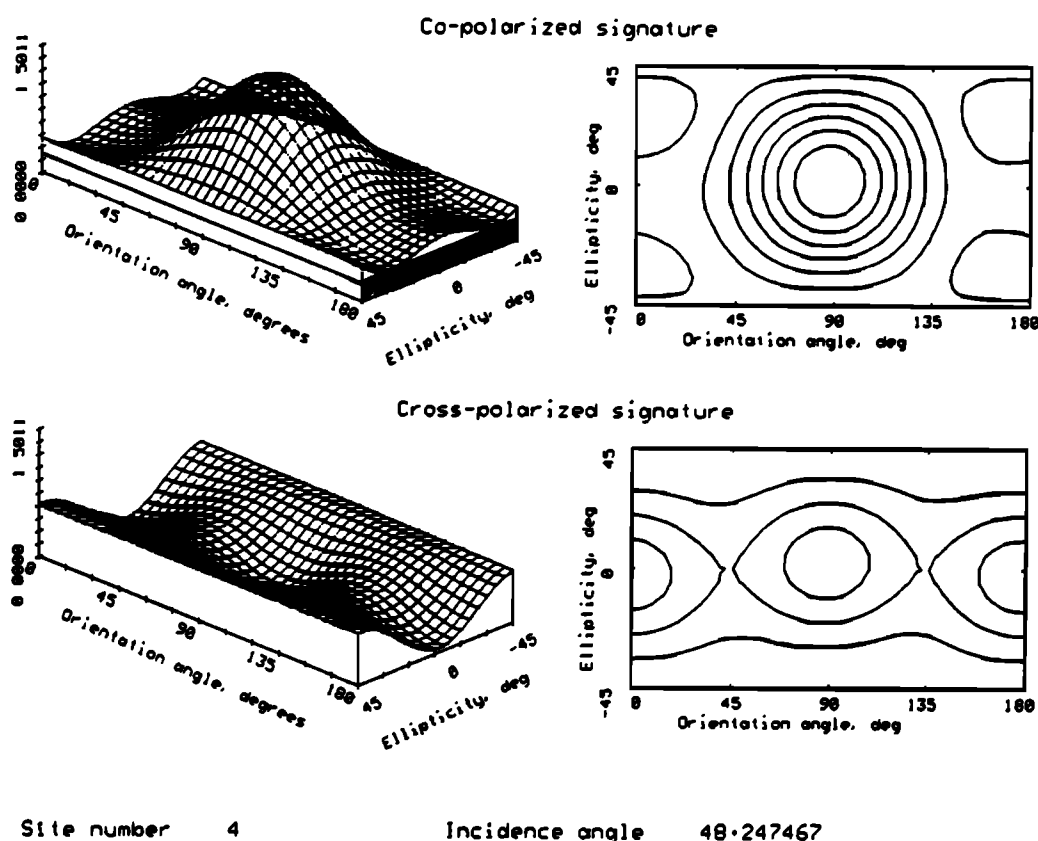


Fig. 3. L band copolarized and cross-polarized signatures extracted from sample 137-4 (thin first-year (ThFY) ice) at an incidence angle of  $48^\circ$ . The signature indicates a typical Bragg scattering example where linear VV-polarized returns form the distinctive unimodal peak in the copolar surface plot. Unpolarized returns constitute the shaded pedestal in the copolarized signature.

depth of several meters. The old ice is relatively pure, and since the dielectric constant of freshwater ice is essentially independent of frequency in the microwave range, this value would apply at each frequency. More realistically however, absorption losses due to minor impurities residing within the ice are likely to reduce penetration to the order of a few meters at P and L band. In the case of C band the size of small inclusions and bubbles within the upper layers of old sea ice becomes significant, and scattering losses will lead to reduced penetration depths of less than 1 m.

Figures 4a and 4b show the distributions of  $r_{HH/VV}$  and  $\Delta\phi_{HH-VV}$ , computed for each pixel (each pixel in the standard compressed data format is a nominal four-look average). In the case of the co-polar phase, we have binned the resulting data into  $10^\circ$  intervals for purposes of clarity in plotting the distributions. Recall from section 3 that our estimated precision for  $\Delta\phi_{HH-VV}$  is  $5^\circ$ . Table 4 gives the mean and standard deviations computed directly from the (unbinned) data to within  $1^\circ$ , allowing the reader to judge the significance of differences in light of the estimated precision.

The immediate impression from these plots is the similarity in signatures between old ice regions, whether the regions occur in the same or separate images. At C band, the HH and VV backscattered power from MY samples within the same image varies by only 3 dB and 2.5 dB, respectively, while at L band the variability in the same channels is a fraction

of a decibel. In Figure 4a one sees that the distribution of  $r_{HH/VV}$  is consistently broader at C band than at L or P band, and in fact that many pixels display a ratio  $r_{HH/VV} > 1$ . That is, for many pixels the backscattered intensity at HH polarization is greater than that at VV polarization. Though the mean of the individual pixel ratios  $\mu_{HH/VV}$  is less than 1 (see Table 4), the mean ratio at C band remains considerably higher than those for the two lower-frequency bands.

For comparison, we have computed a predicted value  $\hat{r}_{HH/VV}$  for the copolar amplitude ratio using one of the simplest possible theoretical backscattering models [Winebrenner et al., 1989]. The result is shown as a vertical line segment in Figure 4a and in parentheses next to  $\mu_{HH/VV}$  in Table 4. The model used is that of first-order Bragg rough surface scattering (i.e., conventional first-order perturbation theory) with a homogeneous half-space of material below the rough ice surface having relative permittivity  $\epsilon_r = 2.9 - j0$  (see Table 2b). Although data on the permittivity of old ice are scarce, this value is reasonable in light of previous work, and the results are quite insensitive to changes in permittivity of even 10% [Winebrenner et al., 1989]. The ratio  $r_{HH/VV}$  is independent of surface roughness in first-order Bragg scattering [Winebrenner et al., 1989] and thus depends only on  $\epsilon_r$  and  $\theta$ . The values shown in Figure 4 and Table 4 are those computed at incidence angles corresponding to the centers of each study region.

TABLE 3. Summary Statistics of Sample Polarization Signature Characteristics

Frequency	Box	Coefficient Variation $\gamma$	Fraction Polarization $f_p$
<i>Beaufort Sea, Scene 137</i>			
C band	1	0.09	0.83
	2	0.05	0.90
	3	0.08	0.86
	4	0.03	0.94
	5	0.04	0.93
L band	1	0.03	0.95
	2	0.03	0.93
	3	0.02	0.96
	4	0.04	0.93
	5	0.04	0.92
P band	1	0.02	0.95
	2	0.05	0.91
	3	0.01	0.97
	4	0.04	0.92
	5	0.05	0.91
<i>Beaufort Sea Scene 183</i>			
C band	1	0.08	0.85
	2	0.05	0.91
	3	0.04	0.93
	4	0.04	0.92
	5	0.10	0.82
L band	1	0.03	0.94
	2	0.02	0.95
	3	0.02	0.96
	4	0.03	0.95
	5	0.02	0.96
P band	1	0.06	0.89
	2	0.04	0.93
	3	0.05	0.91
	4	0.04	0.93
	5	0.01	0.98
<i>Bering Sea Scene 260</i>			
L band	1	0.03	0.93
	2	0.08	0.85
	3	0.09	0.84
	4	0.04	0.93
	5	0.03	0.94

The mean copolar ratio  $\mu_{HH/VV}$  is within 1 standard deviation of the Bragg scattering prediction at each frequency. However, Bragg scattering seems unlikely to be a good explanation for the values observed at C band because of the consistency with which mean values exceed the theoretical value. The HH/VV ratio computed by averaging HH and VV over the study region and computing of the ratio of mean (ensemble averaged) powers is also much larger than Bragg scattering can explain. The measured HH/VV channel offset at C band (see section 3) is not large enough to reconcile the measurements with Bragg scattering theory. However, a contribution from volume scattering from air bubbles in the upper layer of old ice would produce a shift of  $r_{HH/VV}$  toward 1 [Winebrenner *et al.*, 1989]. Indeed, it is widely thought that this is precisely the mechanism causing the bright return from old ice at C band. Thus this C band observation is at least qualitatively consistent with what is generally known about scattering from old ice [Onstott *et al.*, 1987]. From all available examples of MY ice at this wavelength (11 independent samples) the cross-polarized (HV)

backscatter is on average 11.2 dB and 9.8 dB below the VV and HH backscattered power levels, respectively.

The mean value of  $r_{HH/VV}$  at L band is within 8.1% of the Bragg scattering prediction  $\hat{r}_{HH/VV}$  at each frequency. This is consistent with the conventional view that the air bubbles in old ice are too small to scatter efficiently at L band and that backscattering from old ice at this frequency is due mostly to scattering from small-scale surface roughness. The mean value of  $r_{HH/VV}$  at P band is consistently slightly greater than that at L band, though the significance of this is somewhat questionable given the unknown HH-VV channel offset at P band (see section 3). The resulting HV backscatter at L- and P-bands is some 17.1 and 19.6 dB below the VV-polarized backscattered power level. In addition, the mean HV/HH ratio is -13 dB, which is consistent with previous modeling efforts to simulate volume scattering from bubbly low-loss ice with air volume fractions around 5% and mean bubble diameters between 2 and 3 mm [Winebrenner *et al.*, 1989].

The immediate observation from the MY copolar phase distributions is that whereas at L and P bands all sampled distributions have a narrow peak, those at C band are distinctly different and have a much broader spread. Copolar phase distributions from regions 137-3 and 183-5 (Figure 4b) are extremely similar and rather strongly peaked around zero at each frequency, especially at L and P band (thus indicating little variation in copolar phase between old ice regions used for phase calibration and those used for sample signatures). Both Bragg scattering and models for volume scattering from spherical air bubbles give a predicted copolar phase differences in the range  $-6^\circ \leq \phi_{HH-VV} \leq 6^\circ$  in all cases. The distribution of phases in region 137-1 at first sight appears to differ from the other two regions, especially at C band. However, inspection of Table 4 shows that the mean values of copolar phase are virtually identical between all three regions (given the estimated  $5^\circ$  measurement precision). The standard deviation in the observed phase distributions is what differs, and is larger, in region 137-1. Similarly, the value of  $\sigma_{HH/VV}$  is high in comparison with the other examples (especially at C band). Examination of nearly-coincident Ka-band Radiometric Mapping System (KRMS) images does not reveal anything obviously different radiometrically about this old ice region from the other two. However, closer looks at the SAR power images at each frequency indicates a bright linear feature crossing the sample area in 137-1. An increased spread in the copolar amplitude and phase distributions in this region thus seem likely to result from this ridgelike feature and the inherent mixture in the scattering mechanisms.

Finally, note that the fractional polarization  $f_p$  at L and P bands is very high, with values of 0.95 and above (Table 3). This is consistent with the hypothesis of no multiple scattering at these frequencies. The values of  $f_p$  at C band are notably lower, varying between 0.82 and 0.86. This supports the notion of heterogeneity of scattering mechanisms, or the presence of some multiple scattering, most likely volume scattering, in old ice at this frequency. The observed value for  $f_p$  compares well with typical values produced by models that treat multiple scattering from air bubbles in the low-density upper layer [Winebrenner *et al.*, 1989]. However, even the lowest value of 0.82 is much higher than that often seen in cases of scattering from vegetation [Zebker *et al.*, 1987]. Thus old multiyear sea ice is less strongly volume scattering at C band than are some other geophysical media.

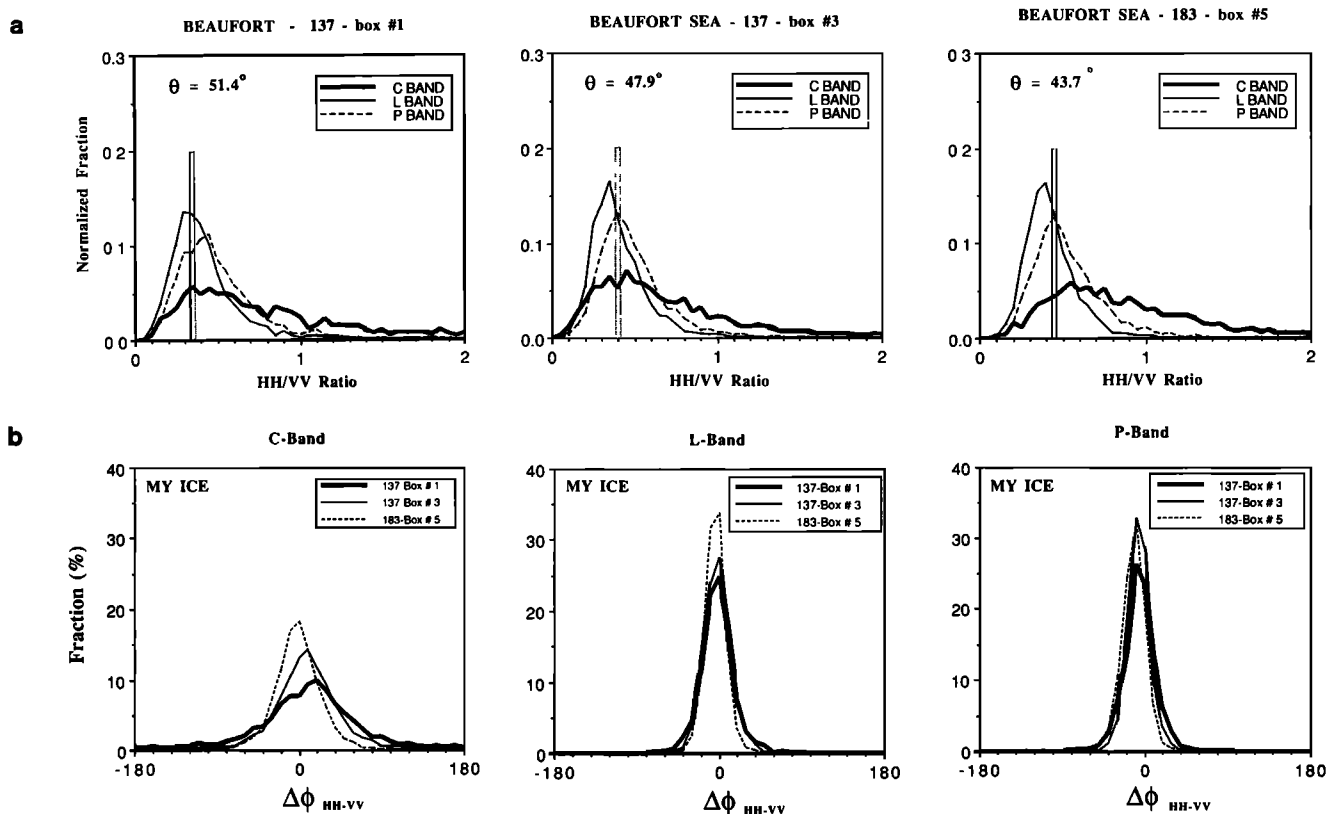


Fig. 4. Normalized MY ice sample distributions extracted from windows in Plates 1 and 2: (a) individual sample copolar amplitude ratio (i.e.,  $r_{HH/VV}$ ) distributions for each frequency and (b) corresponding copolar phase difference distributions for a few examples at each frequency. Summary statistics are shown in Table 4.

### First-Year Ice Signatures

It is convenient to subdivide the FY ice regions into two groups. The first group consists of those regions that, on the basis of morphological clues and brightness in total power images, appear to contain relatively thick first-year ice, i.e., ice of the order of a meter thick. These are regions 137-2, 183-1, and 183-4 in the Beaufort Sea and regions 260-1 and 260-4 in the Bering Sea. The second group consists of those regions that, on the basis of morphology and low backscattered power at L and P bands, appear to contain new ice or open water. These are regions 137-4, 137-5, 183-2 and 183-3 in the Beaufort, and region 260-3 in the Bering. We first discuss signatures of the apparently thicker ice as a group, then those of the apparently thin ice group. We then compare signatures of the two groups.

On the basis of dielectric values given in Table 2, several estimates of the frequency-dependent penetration depths are made. For first-year ice it is assumed that scattering losses due to bubbles can be ignored, and so the values are based upon absorption alone [Onstott *et al.*, 1987]. The calculation leads to a range of estimated penetration depths in thick first-year ice of between 8 cm and 60 cm, for C band through P band, respectively. The equivalent range for new ice is between 5 cm and 32 cm for the shortest to longest wavelengths, respectively. Estimated penetration depths at L band fall between these two values in each case. One further assumption is that in the case of the thick ice the snowcover is essentially dry and transparent to microwaves at these frequencies. The surface characteristics of the thin, young sea ice in the later examples are unknown, but the surface

may comprise a highly saline layer of slush, frost flowers, or salt flowers [Drinkwater and Crocker, 1988], thereby significantly reducing the penetration depth.

**Thick first-year ice.** Consider first the ratios  $r_{HH/VV}$  in regions 137-2, 183-1, and 183-4 (see Figure 5a and Table 4). For comparison, theoretical values of  $r_{HH/VV}$  are computed on the basis of Bragg scattering theory for ice of effectively infinite thickness (i.e., of thickness greater than the penetration depth). These values are shown in parentheses in Table 4 next to the observed mean ratio  $\mu_{HH/VV}$  and are also denoted by a vertical box in Figure 5a. For the ice properties, a bulk ice salinity of 8.5‰ and an ice temperature of  $-10^{\circ}\text{C}$  are assumed. Brine volume fractions were calculated using the equations of Frankenstein and Garner [1967], and the dielectric constant of the ice estimated using the regression equations given by Vant *et al.* [1978]. Although our assumed values of temperature and salinity may differ somewhat from the actual values in the scene,  $r_{HH/VV}$  is relatively insensitive to permittivity and thus to brine volume within the range likely to occur in our images [Winebrenner *et al.*, 1989]. The ratio varies much more strongly with incidence angle; thus we have computed our results at angles corresponding to the centers of the sample regions.

At C band the variability in HH and VV backscattered power for thick first-year (TFY) ice within a scene is 2.6 dB and 4.2 dB, respectively. Generally, the HV backscattered power is about 13.4 dB below the HH and VV levels. Values of  $\mu_{HH/VV}$  at C band are commonly large and close to unity, ranging between 0.81 and 1.18 (Table 4). While the spreads in the ratio distributions ( $\sigma_{HH/VV}$ ) are comparable to those in



TABLE 4. Table of Summary Statistics from Sample Areas in Images 137, 183, and 260

Sample	Type	$\theta$	$\mu_{HH/VV}$	$\sigma_{HH/VV}$	$\mu_{HH/HV}$	$\sigma_{HH/HV}$	$\bar{\phi}_{HH-VV}$	$\sigma_{\phi_{HH-VV}}$
<i>C Band</i>								
137-1	MY	51.43	0.70 (0.36)	1.21	8.84	20.04	8.73	57.34
137-2	TFY	43.13	0.81 (0.43)	1.01	20.40	40.25	1.60	28.53
137-3	MY	47.86	0.57 (0.40)	0.70	8.82	18.47	7.96	39.45
137-4	ThFYa	48.25	0.29 (0.34)	0.51	11.82	21.31	6.01	69.46
137-5	ThFYa	45.15	0.36 (0.38)	0.58	9.04	19.95	7.72	63.05
183-1	TFY	49.29	1.18 (0.35)	1.59	15.37	27.37	8.18	36.46
183-2	ThFYb	43.82	1.00 (0.39)	0.89	25.72	52.70	-1.48	27.27
183-3	ThFYb	40.60	0.91 (0.44)	0.90	33.74	56.97	-4.07	23.06
183-4	TFY	39.03	0.96 (0.49)	1.13	30.97	55.89	2.05	34.82
183-5	MY	43.69	0.79 (0.45)	0.83	9.54	21.92	-1.68	29.39
<i>L Band</i>								
137-1	MY	51.43	0.38 (0.36)	0.29	15.35	33.75	-1.63	19.86
137-2	TFY	43.13	0.52 (0.41)	0.86	16.09	33.80	-10.92	62.99
137-3	MY	47.86	0.37 (0.40)	0.24	21.57	31.26	-1.54	16.00
137-4	ThFYa	48.25	0.27 (0.32)	0.40	6.92	21.88	3.10	66.46
137-5	ThFYa	45.15	0.32 (0.37)	0.33	7.54	14.52	5.45	45.90
183-1	TFY	49.29	0.43 (0.33)	0.60	18.04	31.75	-4.52	41.07
183-2	ThFYb	43.82	0.30 (0.38)	0.69	11.34	16.28	19.66	39.27
183-3	ThFYb	40.60	0.27 (0.42)	0.24	9.86	12.95	17.30	26.41
183-4	TFY	39.03	0.48 (0.48)	0.66	19.27	23.92	-3.12	35.00
183-5	MY	43.69	0.41 (0.45)	0.22	22.96	29.58	-4.05	12.45
260-1	TFY	42.89	0.67 (0.42)	0.94	13.05	11.36	-14.09	14.77
260-2	FYR	41.84	0.80 (0.43)	0.88	8.36	11.40	-7.31	22.68
260-3	ThFY	47.66	0.32 (0.32)	0.51	4.92	8.77	3.82	44.20
260-4	TFY	46.10	0.71 (0.37)	0.51	16.57	21.58	3.64	17.28
260-5	FYR	41.12	0.54 (0.44)	0.31	10.91	13.31	0.86	13.83
<i>P Band</i>								
137-1	MY	51.43	0.46 (0.36)	0.41	26.90	47.98	-5.40	20.70
137-2	TFY	43.13	0.65 (0.40)	1.08	20.79	45.67	8.60	35.72
137-3	MY	47.86	0.45 (0.40)	0.30	48.75	59.44	-6.56	13.42
137-4	ThFYa	48.25	0.29 (0.30)	0.43	6.72	15.05	3.73	52.07
137-5	ThFYa	45.15	0.41 (0.34)	0.60	10.33	24.65	13.37	41.30
183-1	TFY	49.29	0.70 (0.31)	0.95	15.68	29.72	6.59	40.25
183-2	ThFYb	43.82	0.35 (0.36)	0.45	13.21	24.29	3.58	41.84
183-3	ThFYb	40.60	0.41 (0.40)	0.41	11.72	21.02	-4.06	41.80
183-4	TFY	39.03	0.65 (0.46)	0.97	27.57	53.83	-6.55	27.99
183-5	MY	43.69	0.50 (0.45)	0.36	58.14	66.23	-12.35	14.99

Multiyear ice is denoted by MY, and thick and thin FY ice, by TFY and ThFY, respectively. Predicted values of the copolar amplitude ratio,  $\hat{r}_{HH/VV}$ , are denoted in parentheses.

old ice, these mean ratios are considerably larger than those observed for old ice. Such large values are difficult to explain within the framework of the conventional small-perturbation backscattering from slightly rough FY ice. If we assume backscattering from the rough snow-ice interface to be dominant, due to attenuation and lack of volume scatters for C band radiation in FY ice, the horizontal and vertical dimensions of surface roughness elements must be larger than expected relative to the wavelength scale (5.6 cm at C band). Rough surface scattering simulations using the Kirchhoff or physical optics method can be used to explain large values of  $r_{HH/VV}$  [Ulaby *et al.*, 1986; Kuga *et al.*, 1990]. For instance, in the geometric optics scattering limit (when backscattering occurs from tilted portions of the FY ice surface), plane boundary reflection determines that the HH and VV returns should be equal (thus  $r_{HH/VV} \rightarrow 1$ ). It follows that in order to simultaneously explain the lower mean ratios for old ice, we would have to postulate a smoother, more Bragg-scattering-like snow ice interface for old ice than for FY ice. Currently, we have no centimeter-scale surface roughness information which can be used to substantiate this argument.

By contrast to the Beaufort Sea situation at C band, the

mean ratios  $\mu_{HH/VV}$  at L band are more consistent with those predicted by Bragg scattering, and the HH typically is lower than the VV backscattered power by about 3.2 dB. Similarly, the recorded cross-polarized (HV) returns are an average of -15.7 dB below the VV power. As in the case of old ice,  $\mu_{HH/VV}$  at P band (-1.8 dB) is somewhat larger than those at L band, but again the significance of this observation may be small given the uncertainties in P band channel offsets. Note also that the standard deviation  $\sigma_{HH/VV}$  in the observed distributions at L and P bands is much larger for TFY than for old ice. We can offer no immediate explanation for this, but point it out as a stimulus for further work.

In comparison with the thick Beaufort Sea FY ice, the L band distributions in Figure 6 from 260-1 and 260-4 in the Bering Sea are not so consistent with Bragg scattering. Instead, the predicted ratios  $\hat{r}_{HH/VV}$  in Table 4 are lower than those observed by nearly 50%. The mean value of  $\mu_{HH/VV}$  is 0.69 (-1.6 dB), and is likely caused by backscattering from a rougher surface. Also, the HV power has increased to only -13.3 dB below the VV recorded levels. Thus despite apparent similarities in the images in Plates 1-3, the Bering Sea TFY ice floes have a different polarimetric signature when compared with Beaufort Sea examples above. Of note

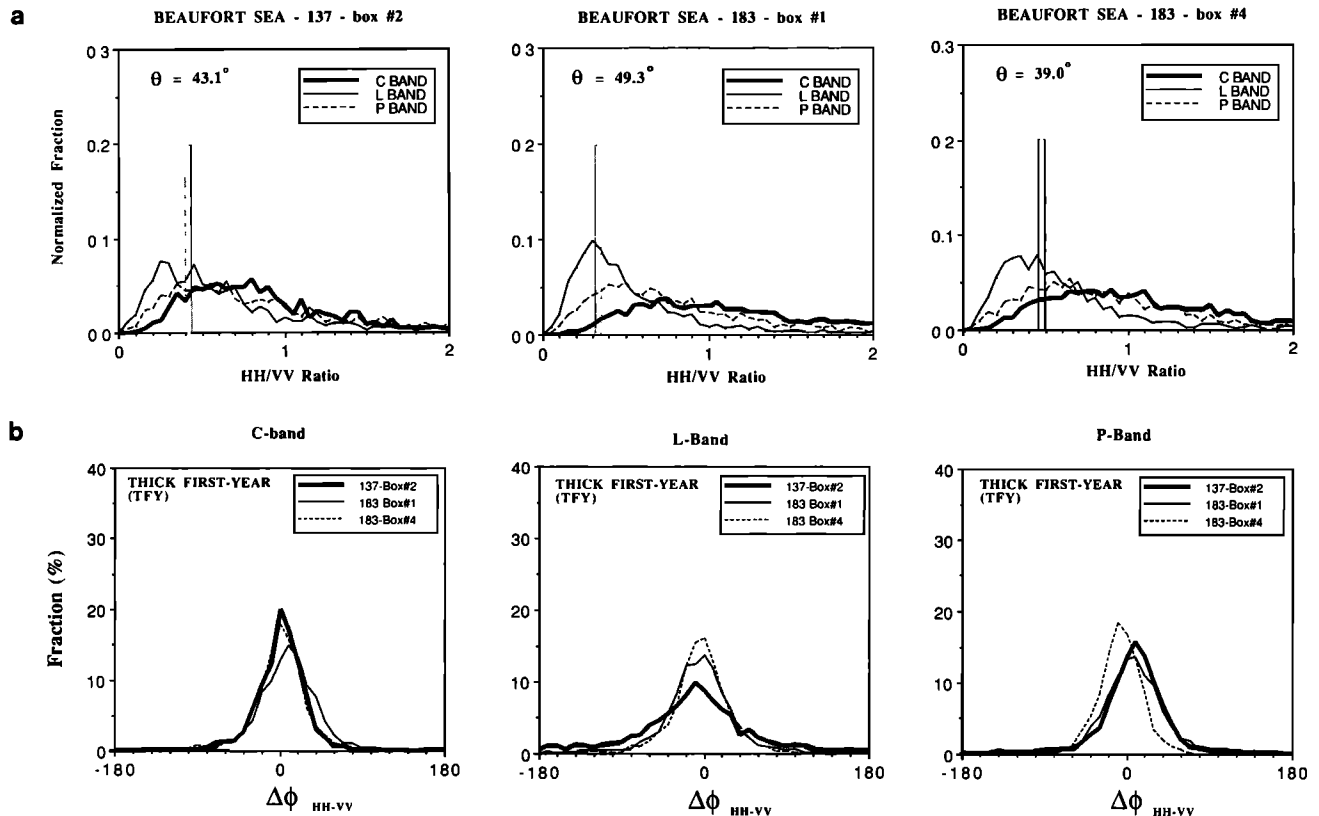


Fig. 5. Normalized thick first-year (TFY) ice sample distributions from Plates 1 and 2: (a) frequency-dependent copolar amplitude ratio (i.e.,  $r_{HH/VV}$ ) distribution for each sample and (b) the corresponding co-polar phase difference distributions. Summary statistics are given in Table 4.

is the fact that these are the highest  $\mu_{HH/VV}$  values observed for undeformed, thick FY ice at this wavelength.

In all examples, the observed fractional polarizations  $f_p$  are approximately the same at L band as were observed in old ice (Table 3). At P band they range between 0.89 and 0.93; these are notably lower than those for old ice. The greatest variations are at C band, where values range from a typical old ice value of 0.85, in region 183-1, to 0.92 in region 183-4. We have not found a ready explanation for these observations, but corresponding increases in the coefficient of variation  $\gamma$  appear to indicate the averaging of signatures from a sample area with varying scattering mechanisms [van Zyl *et al.*, 1987]. Nevertheless,  $\gamma$  is commensurate with low values associated with ocean surface backscattering ( $\gamma \approx 0.05 \pm 0.02$ ). Comparisons with other geophysical media indicate that this variability is minimal: vegetated areas, for instance, were previously observed to produce values of  $\gamma \approx 0.36 \pm 0.11$  [van Zyl *et al.*, 1987].

The behavior of the copolar phase difference  $\Delta\phi_{HH-VV}$  at C band is similar for TFY and old ice (Figure 5b). The standard deviations of the phase distributions at C band (Table 4) differ only negligibly between these ice types. Individual TFY ice regions may at first seem to have mean copolar phases significantly different from old ice. However, examination of the variations in mean copolar phase difference within the group of TFY ice regions indicates that individual variations are within the range of statistical fluctuations.

By contrast, the behavior of  $\Delta\phi_{HH-VV}$  at L and P bands differs somewhat between Beaufort Sea ice types, in that the

width of phase distributions is much broader for TFY ice than for old ice (see Figures 4b and 5b). The sample standard deviations vary by roughly a factor of 3 in most cases. Variations in  $\bar{\phi}_{HH-VV}$  from region to region (Table 4) again appear to be largely due simply to statistical variability. It is curious, nonetheless, that the mean copolar phase in region 137-2 is around 10° lower than that of old ice at both C and L bands. The shift in the other direction at P band, and the lack of such correlation in other FY ice regions, would suggest that the similar C and L band shifts are merely coincidental. However, other statistics from sample 137-2 such as  $\mu_{HH/VV}$  and  $\sigma_{HH/VV}$  demonstrate relatively high values, perhaps indicating that this is a relatively disturbed thick first-year ice surface. Observations from Figure 2 also support that sample 137-2 is chosen in an area of ice which has considerable ridging.

A separate note is made of the phase difference behavior for Bering Sea L-band examples 260-1 and 260-4 in Figure 6b. In these example distributions,  $\Delta\phi_{HH-VV}$  is more similar to the old ice cases in Figure 4 than the thick FY examples in Figure 5b. Typically, these examples have a mean standard deviation of phase difference of 16° compared with the 46.4° recorded in the Beaufort Sea samples. The range of this variability in  $\Delta\phi_{HH-VV}$  requires further explanation, and the source of this variability should be the focus for future modeling studies.

*Thin first-year ice.* Turning to apparently young, thin first-year ice (ThFY), a further subdivision into two sub-groups seems useful on the basis of image scattering characteristics. Regions 137-4 and 137-5 (ThFYa) appear darker

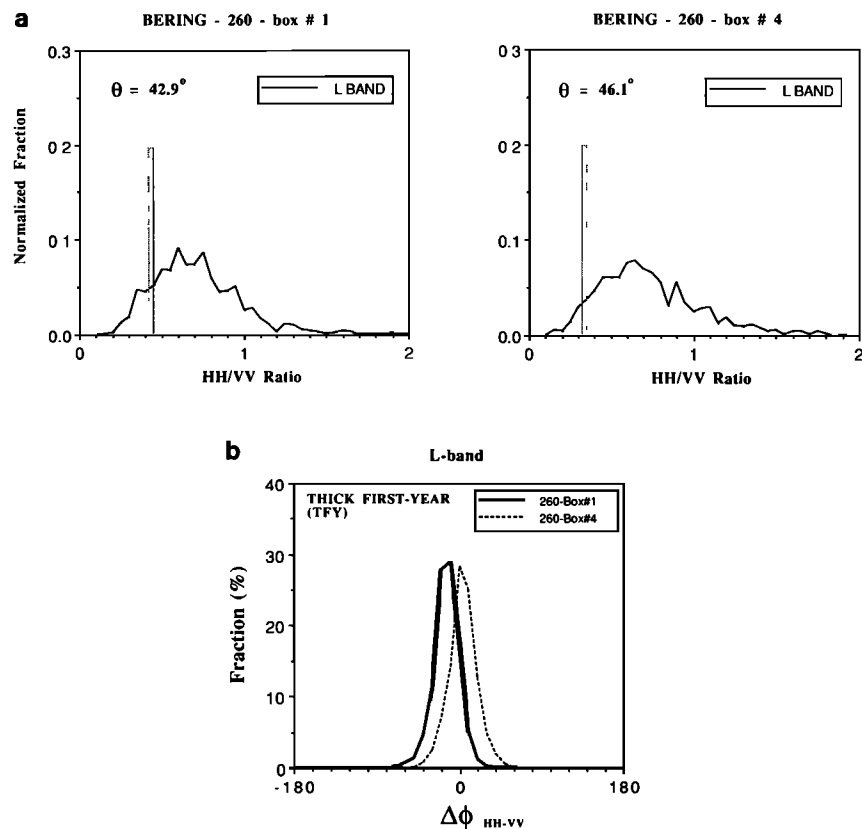


Fig. 6. Normalized Bering Sea thick first-year (TFY) ice sample distributions from Plate 3: (a) copolar amplitude ratio (i.e.,  $r_{HH/VV}$ ) distributions at each frequency and (b) corresponding L band copolar phase difference distributions. Summary statistics are given in Table 4.

than MY ice in power images at all three bands. Judging from coincident KRMS Ka-band passive microwave radiometer data and the style of deformation features, this ice is likely thinner than the older (and thus thicker) FY ice characterized by region 137-2. Though regions 183-2 and 182-3 similarly appear dark at L and P bands, they have anomalously bright backscattered returns at C band which approach and even exceed power levels observed for old ice. For example, the C band VV-polarized power in example 183-3 is some 0.7 dB higher than the equivalent brightest MY ice example in 183-5. For this reason, these two examples are considered unique (and labeled ThFYb).

Polarimetric signatures for these two thin ice subgroups also differ (see Figures 7 and 8). In 137-4 and 137-5, at each frequency, the mean copolar ratios  $\mu_{HH/VV}$  are a little lower than those resulting by Bragg scattering from effectively infinitely thick (i.e., a half space of) new ice (Figure 7a). For comparison, in Table 4 we have shown theoretical ratios  $\hat{r}_{HH/VV}$  in parentheses computed in a similar fashion to those in previous sections, assuming a bulk ice temperature of  $-8^{\circ}\text{C}$  and salinity of 15‰ (Table 2). Values of  $\hat{r}_{HH/VV}$  for open water at these incidence angles also fall well below those mean values observed for this ice (in the range 0.10–0.20), thus supporting the reasoning that it is not open water.

Values of  $r_{HH/VV}$  for 183-2 and 182-3 at L and P bands are essentially indistinguishable from those in 137-4 and 137-5 (Figure 7b). The average values of  $\mu_{HH/VV}$  for these samples together are  $-5.4$  and  $-4.4$  dB for L and P bands, respectively, and at both frequencies the ratio  $\mu_{HH/HV}$  is approxi-

mately 10 dB. However, the C band values of  $r_{HH/VV}$  for 183-2 and 183-3 (1.0 and 0.91) are comparable to those observed at C band in thicker FY ice and are also notably larger than those for old ice. This implies that the thin FY ice surfaces in these examples must appear somewhat rougher than the other TFY ice samples. The variability in mean C band backscattered power for both region 183-2 and 183-3 is 3.5 dB and 3.9 dB at HH and VV polarizations, respectively. This variability is somewhat reduced for regions 137-4 and 137-5, to 2.9 dB and 1.9 dB, respectively. The values of  $\mu_{HH/HV}$  from 137-4 and 137-5 are approximately 4.6 dB higher than the mean ratio of 29.7 observed for examples in scene 183 (Table 4). Nonetheless, generally speaking the C band cross-polarized (HV) returns from 183-2 and 182-3 are of the order of 3 or 4 dB higher than those from the thin ice cases in scene 137. Observations of this unique C band polarimetric response in 183-2 and 183-3 are consistent with previous in-situ microwave observations of frost-flowered surfaces (R. Onstott, personal communication) and measurements of extremely saline salt-flowered, young ice surfaces [Drinkwater and Crocker, 1988].

The fractional polarization of all four Beaufort Sea ThFY samples remains relatively high ( $f_p \geq 0.91$ ) at all frequencies, including C band (Table 3). This is not surprising given that these surfaces are probably relatively saline thin ice (in the range 10–50 cm thick) with a high dielectric constant. Supporting evidence is provided by the onset of divergence in the region surrounding APLIS '88 the previous day. Thus some of the young ice forms such as 183-2 likely formed in the 24-hour period prior to data acquisition on March 11. A



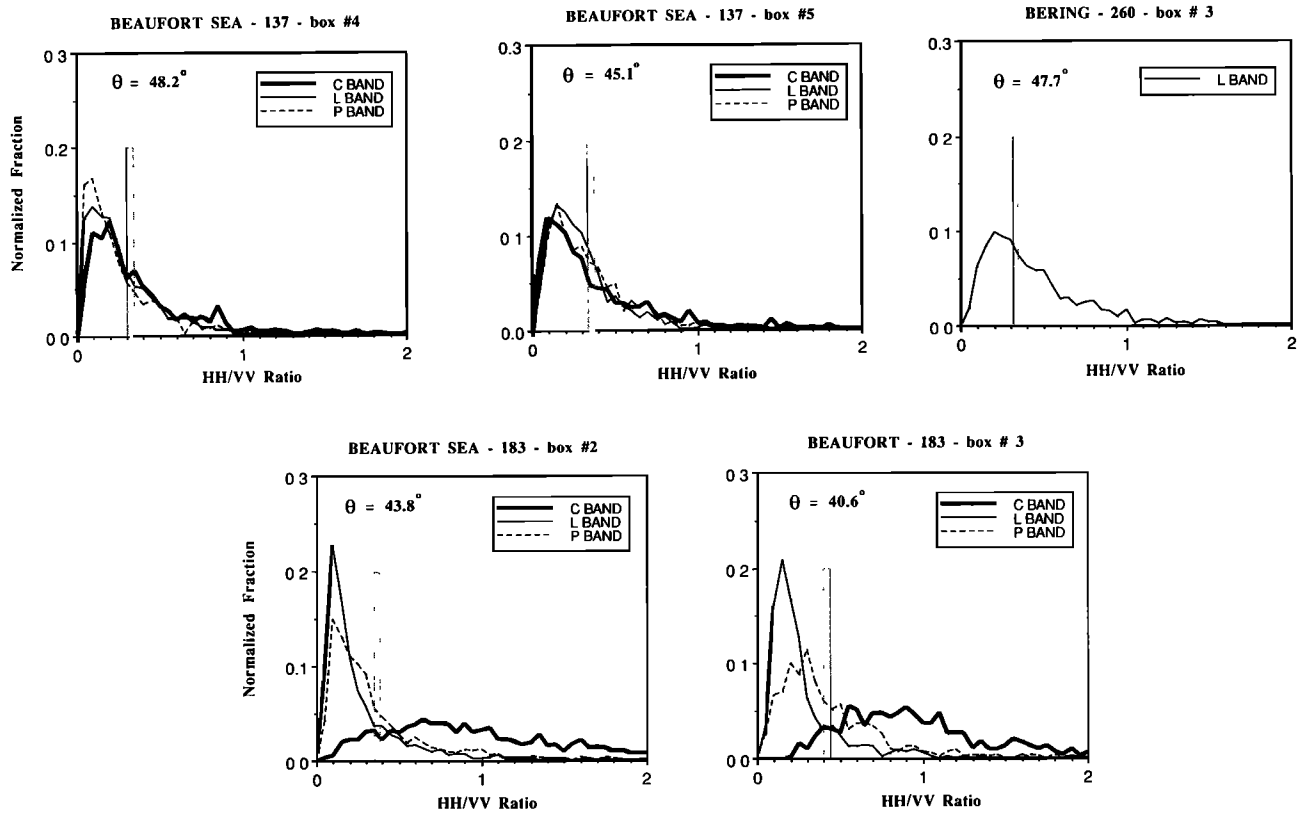


Fig. 7. Three-frequency, normalized copolar amplitude ratio (i.e.,  $r_{HH/VV}$ ) distributions for several examples of thin first-year (ThFY) ice in both the Beaufort and Bering Seas.

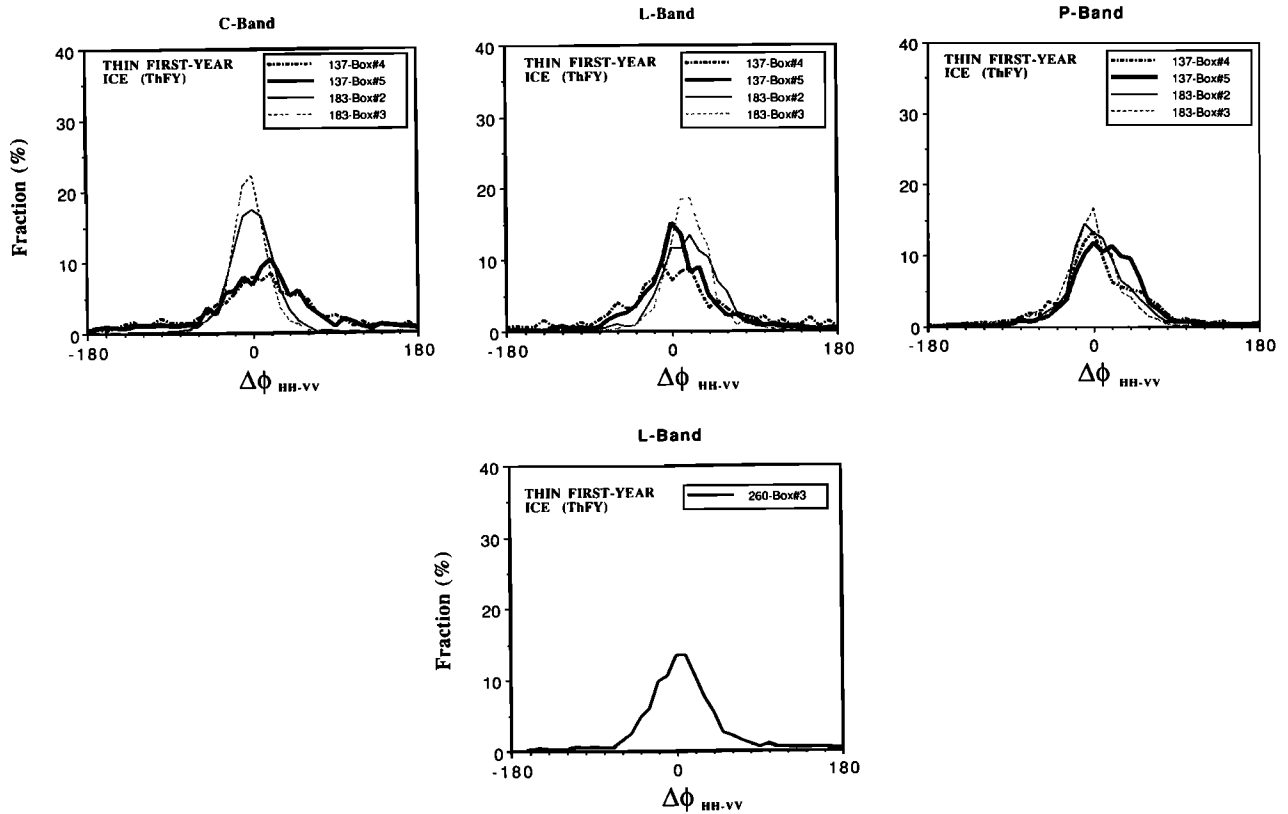


Fig. 8. Thin first-year ice (ThFY) copolar phase difference distributions for examples shown in Figure 7.

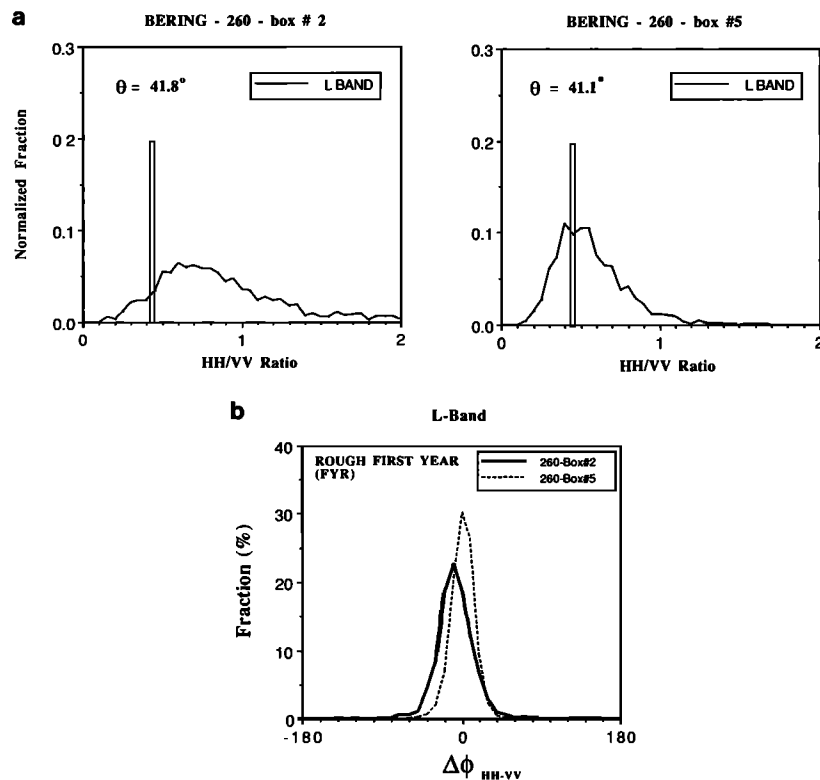


Fig. 9. Examples of observed distributions from samples of deformed Bering Sea ice: (a) Two normalized co-polar amplitude ratio (i.e.,  $r_{HH/VV}$ ) distributions from Figure 2, and (b) the corresponding L band copolar phase difference distributions.

different example of thin young ice from 260-3 in the Bering Sea (Figure 7) demonstrates a mean L band ratio which is predicted exactly by Bragg scattering theory. However, in contrast it has a rather low fractional polarization. Table 3 indicates that 260-3 has the lowest L band value of  $f_p$  observed throughout the data set, and further investigation of the imagery reveals that the surface has considerable structure to it. The accompanying high value of  $\gamma = 0.09$  in Table 3 is an additional indication that the sample includes pixels with rather different scattering properties. This surface may therefore have patches of wet and dry surface which cause some depolarization of the scattered signal.

Mean copolar phase differences at C band in Figure 8 indicate no appreciable shift from those near-zero means of old ice in any of the four thin ice regions. The values of  $\sigma\phi_{HH-VV}$  in regions 183-2 and 183-3 are also comparable to those for old ice (Table 4), while those in regions 137-4 and 137-5 are much larger than for either of the thicker ice types. P band copolar phase differences show some variability between thin ice areas but tend to bracket the values observed for thicker FY ice and show no clear link with morphology as observed in images of backscattered power. The spread of the P band  $\Delta\phi_{HH-VV}$  distributions are comparable to those of thicker FY ice, as are those of the L band distributions. However, the L band values of  $\bar{\phi}_{HH-VV}$  of each of the thin ice regions fall up to  $15^\circ$  and  $20^\circ$  above those of thicker FY ice in the same image. The shift in comparison with old ice is smaller in image 137; FY and MY ice show a  $10^\circ$  difference in this image attributed above to statistical variability. Nonetheless, the size and regularity of this shift seem significant and cannot be explained by any theory we

know of for effectively infinitely thick ice. These results illustrate that the mechanisms for and causes of copolar phase differences warrant further study.

#### Deformed Bering Sea Ice

Deformed ice in the Bering Sea displays significantly different signatures to be considered separately here. This ice type appears in image 260 (Plate 3) as bright areas of textured surface. Such ice has been observed previously by SAR in the Labrador Sea and Beaufort-Chukchi Sea ice margins [Livingstone and Drinkwater, 1991; Drinkwater, 1989; Carsey and Pihos, 1989]. The L-band signature in 260 2, for example, is thought to be caused by rough surface scattering from a well-deformed, rough FY ice surface. Since temperatures were sufficiently cold for ice formation to take place in leads, surfaces are not expected to be undergoing melting. However, wave action and floe interactions in the marginal ice zone often result in ice floe surfaces becoming wetted by salt spray or wave flooding [Bauer and Martin, 1980]. Surface scattering, as a result, is likely to dominate the signatures.

Figure 9a illustrates two copolar ratio distributions, extracted from samples 260-2 and 260-5, along with Bragg scattering copolar ratio predictions denoted by vertical boxes. The former sample, in particular, shows a larger spread of values than is observed in any other L band sea ice example noted, having a mean ratio  $\mu_{HH/VV}$  of 0.8 (Table 4), with a tail extending to high values. The corresponding ratio of mean VV and HV backscattered power is 10.2 dB. This signature appears the result of an extremely rough surface

with a large rms slope. In contrast, the shape of the distribution in 260-5 is more typical of those examples from thick FY ice illustrated in previous sections. Similarly, the value of  $\mu_{HH/VV}$  (0.54) for 260-5 is greater than the theoretical estimate  $\hat{r}_{HH/VV}$  (0.44), also indicating a greater degree of surface roughness than could be accounted for using small perturbation scattering theory.

From the characteristics of the copolar ratio distribution plots which accompany these results in Figure 9a, it appears that physical optics scattering occurs at the roughness scales typical of these ice forms. This would account for the high mean ratios and extended tail in the 260-2 sample distribution. Recent modeling efforts with alternative Kirchhoff physical optics formulations have demonstrated some success in simulating backscattering cross sections of rough ice in the Labrador Sea marginal ice zone [Livingstone and Drinkwater, 1991] using measured centimeter-scale surface roughness statistics.

The mean values of  $r_{HH/VV}$  in samples 260-2 and 260-5 are the two largest observed at L band, thus supporting the argument that these surfaces are in general rougher than the FY ice examples from the Beaufort Sea. There is also an increase in the cross-polarized returns in each case with a typical mean ratio  $\mu_{HH/HV}$  of around  $-10$  dB, perhaps indicating an increase in the importance of second-order surface scattering effects. Notably, the value of  $f_p$  falls to its lowest value 0.85 in 260-2, indicating that depolarization and the relatively higher pedestal could be the result of multiple surface scattering. The higher fractional polarization of returns from 260-5 at a more typical value of  $f_p = 0.94$  is an indication that depolarization is somewhat less important in this case.

Copolar phase difference distributions shown in Figure 9b indicate that 260-2 and 260-5 are similar in characteristics to the Bering Sea TFY ice examples. Values of  $\sigma\phi_{HH-VV}$  for this rough Bering Sea ice are most similar to values recorded for Beaufort Sea MY ice, generally falling in the range  $10^\circ$ – $20^\circ$ . There are, however, significant differences between these values and those recorded for Beaufort Sea TFY ice, and it is concluded that there must be significant structural differences between the two. Variations in phase difference spread at L band are supposedly linked with the relative dominance of a particular scattering mechanism and the fabric of the surface medium and they warrant further investigation.

## 5. DISCUSSION

The preceding sections summarized the polarimetric behavior of each ice type in the three frequencies. Attempts to correlate the observations with the expected microwave responses of the ice types were provided and will not be reiterated here. Here we examine and summarize the salient features observed in the polarimetric measurements of each main ice type at each frequency. Figure 10 shows the polarimetric signatures of the four dominant ice types (MY ice, thick FY ice, and the two subcategories of thin young FY ice) at C, L, and P band. In each summary plot, all Beaufort Sea sample points from Table 4 are displayed in four clusters by ice type. Within each cluster, the frequency-dependent shift in the polarimetric parameter for a particular sample is denoted by a line joining the symbols in a C, L,

P-band sequence. Figure 10 does not indicate the spectral trend for Bering Sea ice because only L band images from these data were suitable for analysis.

Figure 10a illustrates a characteristic increase in  $\mu_{HH/VV}$  from old ice to thick first-year ice and then a contrasting decrease for thin FY ice in all but the anomalously bright C band examples 183-2 and 183-3. It is also evident that if correction factors of  $-1.8$  dB and  $+0.6$  dB were simply added to the C and L band ratios to account for the  $r_{HH/VV}$  channel imbalances (discussed in section 3), there would also be a smearing of the characteristic V shape shown here. Removal of the offsets may therefore result in a trend more consistent with a reduction in the  $\mu_{HH/VV}$  with increasing wavelength. Both subclasses of thin or younger FY ice consistently exhibit the lowest  $r_{HH/VV}$  ratios at L and P bands of all ice types, as can be expected of Bragg scattering from these high dielectric surfaces. However, those surfaces with anomalously high C band backscatter demonstrate mean ratios close to 0 dB. The  $\mu_{HH/VV}$  measurements within each ice type are fairly tightly clustered at all three frequencies. The largest variability occurs at C band with a spread of 1.6 dB for thick FY ice and 1.4 dB for MY ice.

The behavior described above is also observed to some degree in the other polarimetric parameters. At C band, the observed variability in the  $\mu_{HH/VV}$  measurements in MY ice is mirrored in the standard deviation of the copolar phase differences,  $\sigma\phi_{HH-VV}$  (Figure 10b). This range of variability of around  $28^\circ$  at C band is considerably higher than is observed in the other ice types at this wavelength (with the only equivalent spread occurring in TFY ice samples at L band). Such C-band variability could be due to the sensitivity of the shorter wavelengths to anisotropy of inhomogeneities in this volume scattering medium. Generally, if the C-band MY ice points are excluded, the standard deviation of phase difference measurements show increases from MY to TFY to ThFYa ice (i.e., with decreasing ice thickness). Also, excluding the high L band value of  $62.99^\circ$  in the thick first-year ice group (which was attributed in the preceding section to ridged ice), the measurements for these three categories generally indicate a negative spectral trend (i.e., decreasing  $\sigma\phi_{HH-VV}$  with increasing wavelength). In direct contrast, the ThFY ice signatures in subcategory b of Figure 10b show a reversed positive spectral trend from the other classes, with an increase in  $\sigma\phi_{HH-VV}$  with increasing wavelength.

The fractional polarization shown in Figure 10c stays relatively constant over all ice types at L or P bands; however, this parameter is considerably lower in the old ice at C band. A dramatic increase is observed in the transition from C band to the lower frequencies in both MY and thick FY ice. It is interesting to point out that this does not apply in the case of new ice, where the fractional polarization is high in those areas of anomalously bright returns.

It can be seen therefore that there is good separability between these polarimetric features ( $\mu_{HH/VV}$ ,  $\sigma\phi_{HH-VV}$  and  $f_p$ ). From a discrimination point of view these are significant characteristics that could be utilized for separation of different ice types. At this stage it is difficult to explain why the L band copolar ratio variability changes so dramatically between ice type, although there appears to be some relationship with apparent ice thickness.



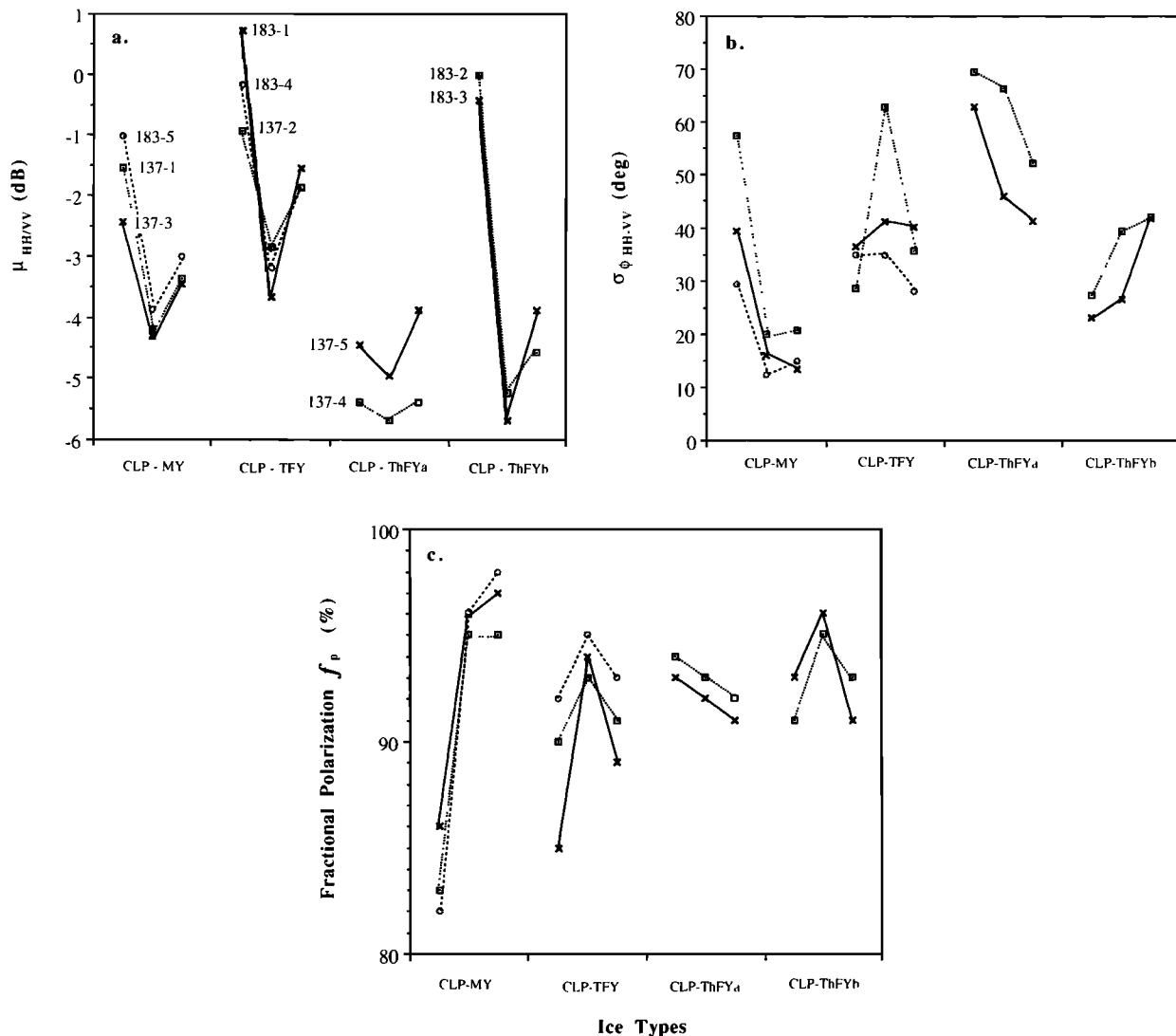


Fig. 10. Summary plots of the spectral trends in (a)  $\mu_{HH/VV}$  (b)  $\sigma_{\phi_{HH,VV}}$ , and (c)  $f_p$  for multiyear (MY), thick first-year (TFY), and two classes of thin first-year (ThFY) ice. Signature values from Table 4 are plotted sequentially at C, L, and P band with a linestyle denoting the frequency trend. Similar symbols are used in each plot to represent the ice samples annotated in Figure 10a. The radiometric accuracy in  $\mu_{HH/VV}$  (estimated from calibrations) is  $\pm 0.8$  dB,  $\pm 0.4$  dB, and  $\pm 2.4$  dB for C, L, and P band respectively. Constant (long-term) offsets in the HH and VV channels are treated in section III. Error terms in Figures 10b and 10c vary and are dependent upon the value of the backscatter for each target with respect to the system noise floor.

## 6. CONCLUSIONS

We have presented a sample of sea ice observations from an examination of the multichannel SAR data set acquired in March 1988. It is shown that the microwave backscatter characteristics of sea ice can now be imaged and recorded simultaneously at three frequencies in any polarization combination desired. Although only a few examples are presented, examination of other data indicates these signatures to be representative of first-year and old ice mixtures in the Beaufort Sea and marginal ice in the Bering Sea at this time of the year. Evidently, there are within- and between-scene consistencies in the signatures from some ice types. Similarly, there are variations brought about by real spatial variability in snow and ice properties. The major advantages of this new tool are that various combinations of wavelength and polarization enhance our capability to distinguish between sea ice of different fabrics or morphology. This extra

capability can be exploited to take advantage of the characteristic microwave responses to these physical properties variations.

At this stage of these early investigations, results suggest that such a polarimetric SAR tool will advance our current ability to extract sea ice geophysical information from microwave images. The P band radar is a particularly interesting addition to the arsenal of instruments for use in microwave remote sensing studies of sea ice because of its increased penetration into more saline ice, and thus warrants further detailed studies. It is imperative, though, that future experiments be conducted in order to coordinate surface measurement with airborne data acquisition, so that the techniques being developed to extract information from polarimetric SAR images can be validated. These experiments should, in light of recent experience, incorporate a comprehensive field calibration exercise in order to remove

cross-channel imbalances and phase offsets and to obtain absolute values of  $\sigma^0$ .

Obviously, other polarimetric features can be explored for characterizing the microwave scattering behavior of sea ice, beyond those utilizing contemporary microwave data which are limited in both frequency and polarization. It is recognized that more work is required in view of the interesting observations and peculiarities that this analysis has provided. Future investigations should incorporate detailed comparisons between the results of theoretical model predictions and the observed polarimetric signatures. Such analyses will highlight geophysical properties of sea ice which have unique polarimetric attributes.

**Acknowledgments.** M.R.D., R.K., and E.R. performed this work in the Polar Oceanography Group and the Radar Science and Engineering Section at the Jet Propulsion Laboratory, California Institute of Technology, under contract to the Oceanic Processes Branch of the National Aeronautics and Space Administration. D.W. performed this work at APL, University of Washington, under a separate NASA contract, NAGW-1256. Thanks go to Joanne Shimada for her help in generating image statistics and graphics and to Ben Holt, Frank Carsey, and John Crawford at JPL for organizing the DC-8 flight series, securing data processing and analysis, and for reviewing the text. The invaluable supporting evidence provided by Duane Eppler and Dennis Farmer (at NOARL) with corresponding KRMS image data, is also recognized.

# REFERENCES

- Bauer, J., and S. Martin, Field observations of the Bering Sea ice edge properties during March 1979, *Mon. Weather Rev.*, 108, 2045-2056, 1980.
- Bredow, J., S. P. Gogineni, A. J. Gow, P. F. Blanchard, and R. K. Moore, Radar backscattering from artificially grown sea ice, *IEEE J. Oceanic Eng.*, OE-14, 259-264, 1989.
- Burns, B. A., SAR image statistics related to atmospheric drag over sea ice, *IEEE Trans. Geosci. Remote Sens.*, GE-28(2), 158-165, 1990.
- Burns, B. A., D. J. Cavalieri, M. R. Keller, W. J. Campbell, T. C. Grenfell, G. A. Maykut, and P. Gloersen, Multisensor comparison of ice concentration estimates in the marginal ice zone, *J. Geophys. Res.*, 92, 6843-6856, 1987.
- Campbell, W. J., W. F. Weeks, R. O. Ramseier, and P. Gloersen, Geophysical studies of floating ice by remote sensing, *J. Glaciol.*, 15(73), 305-328, 1975.
- Carsey, F., and B. Holt, Beaufort-Chukchi ice margin data from Seasat: Ice motion, *J. Geophys. Res.*, 92, 7163-7172, 1987.
- Carsey, F. D., and G. Piliros, Beaufort-Chukchi Seas summer and fall ice margin data from Seasat: Conditions with similarities to the Labrador Sea *IEEE Trans. Geosci. Remote Sens.*, 27(5), 541-551, 1989.
- Cavalieri, D. J., NASA sea ice and snow validation program for the DMSP SSM/I: NASA DC-8 flight report, *NASA Tech. Memo.*, 100706, 1988.
- Cavalieri, D. J., P. Gloersen, and T. T. Wilheit, Aircraft active and passive microwave observations of the Bering Sea ice cover during MIZEX West, *IEEE Trans. Geosci. Remote Sens.*, GE-24, 368-377, 1986.
- Cavalieri, D. J., J. P. Crawford, M. R. Drinkwater, D. T. Eppler, L. D. Farmer, R. R. Jentz, and C. C. Wackerman, Aircraft active and passive microwave validation of sea ice concentration from the Defense Meteorological Satellite Program special sensor microwave imager, *J. Geophys. Res.*, in press, 1991.
- Curlander, J. C., B. Holt, and K. J. Hussey, Determination of sea ice motion using digital SAR imagery, *IEEE J. Oceanic Eng.*, OE-10(4), 358-367, 1985.
- Drinkwater, M. R., LIMEX '87 ice surface characteristics; Implications for C-band SAR backscatter signatures, *IEEE Trans. Geosci. Remote Sens.*, GE-27(5), 501-513, 1989.
- Drinkwater, M. R., Multi-frequency imaging radar polarimetry of sea ice, in *Ice Technology for Polar Operations*, edited by T. K. S. Murthy, J. G. Paren, W. M. Sackinger, and P. Wadhams, pp. 365-376, Computational Mechanics Publications, Southampton, England, 1990.
- Drinkwater, M. R., and G. B. Crocker, Modelling changes in the dielectric and scattering properties of young snow-covered sea ice at GHz frequencies, *J. Glaciol.*, 34(118), 274-282, 1988.
- Drinkwater, M. R., and V. A. Squire, C-band SAR observations of marginal ice zone rheology in the Labrador Sea, *IEEE Trans. Geosci. Remote Sens.*, GE-27, 522-534, 1989.
- Drinkwater, M. R., R. Kwok, and E. Rignot, Synthetic aperture radar polarimetry of sea ice, in Proceedings, IGARSS '90, vol. 2, Cat. No. 90CH2825-8, pp. 1525-1528, IEEE, New York, 1990.
- Drinkwater, M. R., J. P. Crawford, D. J. Cavalieri, B. Holt, and F. D. Carsey, Comparison of active and passive microwave signatures of Arctic sea ice, *JPL Tech. Publ.*, 90-56, pp. 29-36, 1991.
- Evans, D. L., T. G. Farr, J. J. van Zyl, and H. A. Zebker, Radar polarimetry; Analysis tools and applications, *IEEE Trans. Geosci. Remote Sens.*, GE-26, 774-789, 1988.
- Fily, M., and D. A. Rothrock, Extracting sea ice data from satellite SAR imagery, *IEEE Trans. Geosci. Remote Sens.*, GE-24, 849-854, 1986.
- Fily, M., and D. A. Rothrock, Opening and closing of sea ice leads: Digital measurements from synthetic aperture radar, *J. Geophys. Res.*, 95, 789-796, 1990.
- Frankenstein, G., and R. Garner, Equations for determining the brine volume of sea ice from -5°C to -22°C, *J. Glaciol.*, 6(48), 943-944, 1967.
- Freeman, A., A calibration and image quality assessment of the NASA/JPL aircraft SAR during spring 1988, *JPL Tech. Rep.*, D-7197, 60 pp., Jet Propul. Lab., Calif. Inst. of Technol., Pasadena, 1990.
- Grenfell, T. C., Surface-based passive microwave observations of sea ice in the Bering and Greenland seas, *IEEE Trans. Geosci. Remote Sens.*, GE-24, 378-382, 1986.
- Holt, B., R. Kwok, and E. Rignot, Ice classification algorithm development and verification for the Alaska SAR facility using aircraft imagery, in Proceedings, IGARSS '89, vol. 2, Cat. No. 89CH2768-0, pp. 751-754, IEEE, New York, 1989.
- Holt, B., R. Kwok, and E. Rignot, Status of the ice classification algorithm in the Alaska SAR facility geophysical processor system, in Proceedings, IGARSS '90, vol. 3, Cat. No. 90CH2825-8, pp. 2221-2224, IEEE, New York, 1990.
- Kuga, Y., M. W. Whitt, K. C. McDonald, and F. T. Ulaby, Scattering models for distributed targets, in *Radar Polarimetry for Geoscience Applications*, edited by F. T. Ulaby, and C. Elachi, pp. 111-190, Artech House, Norwood, Mass., 1990.
- Kwok, R., J. C. Curlander, R. McConnell, and S. S. Pang, An ice-motion tracking system at the Alaska SAR facility, *IEEE J. Oceanic Eng.*, 15(1), 44-54, 1990.
- Leberl, F., J. Raggam, C. Elachi, and W. J. Campbell, Sea ice motion measurements from Seasat SAR images, *J. Geophys. Res.*, 88, 1915-1928, 1983.
- Lim, H. H., A. A. Swartz, H. A. Yueh, J. A. Kong, R. T. Shin, and J. J. van Zyl, Classification of Earth terrain using polarimetric synthetic aperture radar images, *J. Geophys. Res.*, 94, 7049-7057, 1989.
- Livingstone, C. E., and M. R. Drinkwater, Springtime C-band SAR backscatter signatures of Labrador Sea marginal ice: Measurements vs modelling predictions, *IEEE Trans. Geosci. Remote Sens.*, GE-29(1), 29-41, 1991. (Correction, *IEEE Trans. Geosci. Remote Sens.*, 29(3), 472, 1991.)
- Martin, S., B. Holt, D. J. Cavalieri, and V. Squire, Shuttle imaging radar B (SIR-B) Weddell Sea ice observations: A comparison of SIR-B and scanning multichannel microwave radiometer ice concentrations, *J. Geophys. Res.*, 92, 7173-7179, 1987.
- MIZEX-West Study Group, MIZEX-West: Bering Sea marginal ice zone experiment, *Eos Trans. AGU*, 64, 578-579, 1983.
- Onstott, R. G., T. C. Grenfell, C. Mätzler, C. A. Luther, and E. A. Svendsen, Evolution of microwave sea ice signatures during early summer and midsummer in the marginal ice zone, *J. Geophys. Res.*, 92, 6825-6835, 1987.
- Ramseier, R. O., P. Gloersen, W. J. Campbell, and T. C. Chang, Mesoscale description for the principal Bering Sea Ice Experiment in U.S.S.R./U.S.A. Bering Sea Ice Experiment, in *Proceedings, Symposium on the Joint U.S.S.R./U.S.A. Bering Sea Ex-*

- periment, edited by K. Ya. Kondratyev, pp. 234–269, Gidrometeoizdat, Leningrad, 1975.
- Ulabay, F. T., and C. Elachi (Eds.), *Radar Polarimetry for Geoscience Applications*, 364 pp., Artech House, Norwood, Mass., 1990.
- Ulabay, F. T., R. K. Moore, and A. K. Fung, *Microwave Remote Sensing, From Theory to Applications*, vol. 3, 2162 pp., Artech House, Norwood, Mass., 1986.
- Vant, M. R., R. O. Ramseier, and V. Makios, The complex dielectric constant of sea ice at frequencies in the range 0.1–40 GHz, *J. Appl. Phys.*, 49(3), 1264–1280, 1978.
- van Zyl, J. J., Unsupervised classification of scattering behavior using radar polarimetry data, *IEEE Trans. Geosci. Remote Sens.*, GE-27(1), 36–45, 1989.
- van Zyl, J. J., and H. A. Zebker, Imaging radar polarimetry, in *Polarimetric Remote Sensing*, vol. 3, *Progress in Electromagnetics Research*, edited by J. A. Kong, pp. 277–326, Elsevier, New York, 1990.
- van Zyl, J. J., H. A. Zebker, and C. Elachi, Imaging radar polarization signatures, *Radio Sci.*, 22, 529–543, 1987.
- Wen, T., W. J. Felton, J. C. Luby, W. L. J. Fox, and K. L. Kientz, Environmental measurements in the Beaufort Sea, Spring 1988, *Tech. Rep.*, APL-UW TR 8822, 34 pp., Appl. Phys. Lab., Univ. of Wash., Seattle, 1989.
- Winebrenner, D. P., L. Tsang, B. Wen, and R. West, Sensitivities for two polarimetric backscattering models for sea ice to geophysical parameters, paper presented at Advanced Research Workshop on Direct and Inverse Methods in Radar Polarimetry, N. Atl. Treaty Organ., Bad Windsheim, Germany, Sept. 19–23, 1988.
- Winebrenner, D. P., L. Tsang, B. Wen, and R. West, Sea-ice characterization measurements needed for testing of microwave remote sensing models, *IEEE J. Oceanic Eng.*, 14(2), 149–158, 1989.
- Zebker, H., and Y.-L. Lou, Phase calibration of imaging radar polarimeter Stokes matrices, *IEEE Trans. Geosci. Remote Sens.*, 28(2), 246–252, 1990.
- Zebker, H. A., J. J. van Zyl, and D. N. Held, Imaging radar polarimetry from wave synthesis, *J. Geophys. Res.*, 92, 683–701, 1987.
- M. R. Drinkwater, R. Kwok, and E. Rignot, Jet Propulsion Laboratory, California Institute of Technology, 4800 Oak Grove Drive, Pasadena, CA 91109.
- D. P. Winebrenner, Polar Science Center, Applied Physics Laboratory, HN-10, 1013 NE 40th Street, University of Washington, Seattle, WA 98195.

(Received January 9, 1991;  
revised July 1, 1991;  
accepted July 15, 1991.)